Individual effects of atmospheric water vapor and carbon dioxide on the kinetics of the thermal decomposition of granular malachite

Yuta Aoki and Nobuyoshi Koga*

Department of Science Education, Division of Educational Sciences, Graduate School of Humanities and Social Sciences, Hiroshima University, 1-1-1 Kagamiyama, Higashi-Hiroshima 739-8524, Japan.

Contents

* Corresponding author: e-mail: nkoga@hiroshima-u.ac.jp

S1. Influence of atmospheric water vapor and CO_2

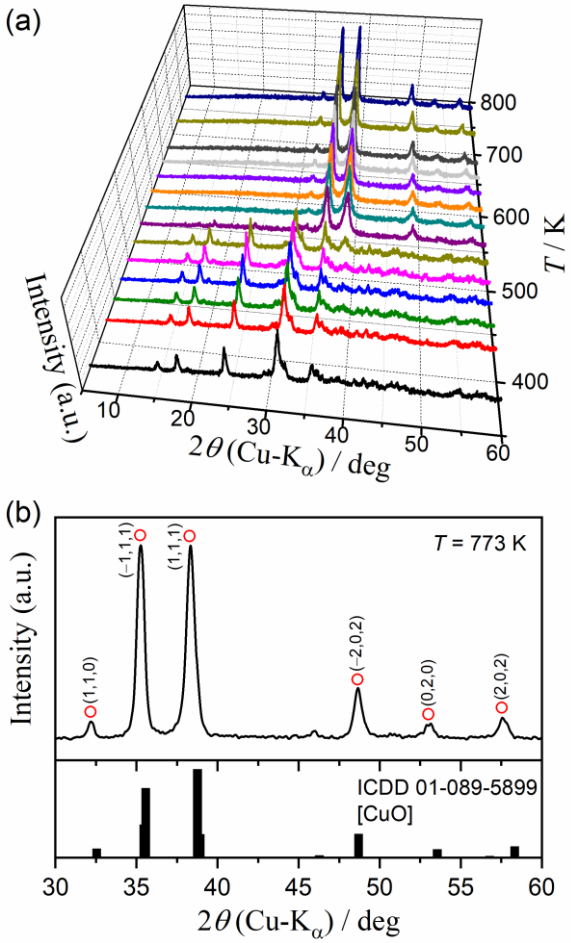

Figure S1. Changes in the XRD pattern when heating granular malachite using a stepwise isothermal heating program in a N_2–H_2O mixed gas stream characterized by $p(H_2O)$ = 2.4 kPa (q_v = 100 cm^3 min^{-1}): (a) Changes in the XRD pattern with temperature and (b) XRD pattern at 773 K.

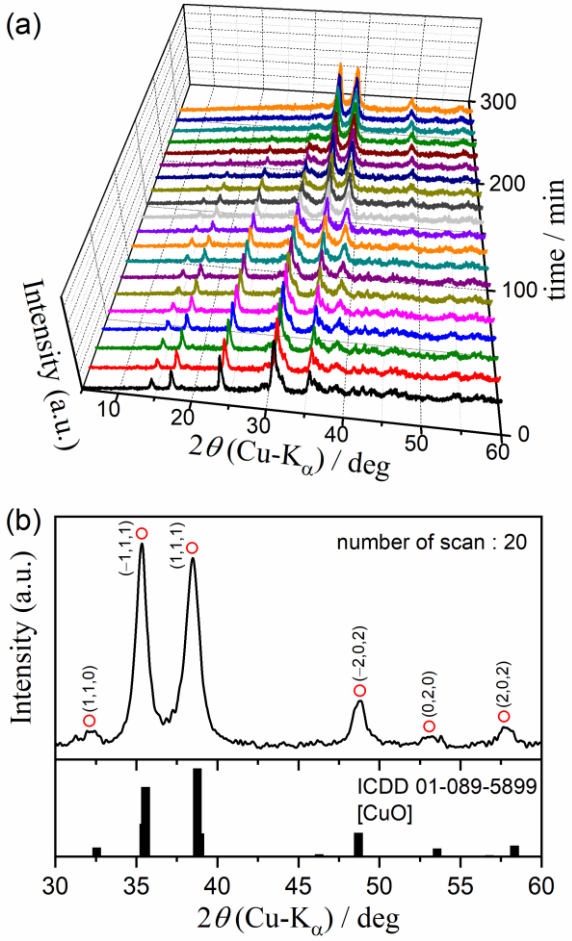

Figure S2. Changes in the XRD pattern when heating granular malachite at 498 K in a N_2–H_2O mixed gas stream characterized by $p(H_2O)$ = 2.4 kPa (q_v = 100 cm^3 min^{-1}): (a) Changes in the XRD pattern with duration and (b) XRD pattern after heated for 285 min.

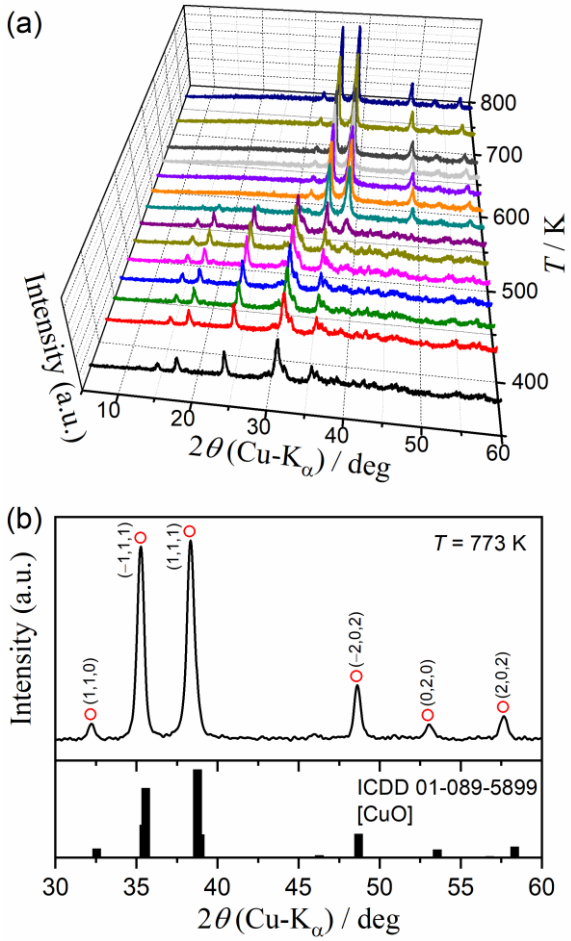

Figure S3. Changes in the XRD pattern during heating the granular malachite using a stepwise isothermal heating program with 15 min isothermal holding sections in a stream of CO_2 gas characterized by $p(CO_2)$ = 100 kPa (q_v = 100 cm^3 min^{-1}): (a) Changes in the XRD pattern with temperature and (b) XRD pattern at 773 K.

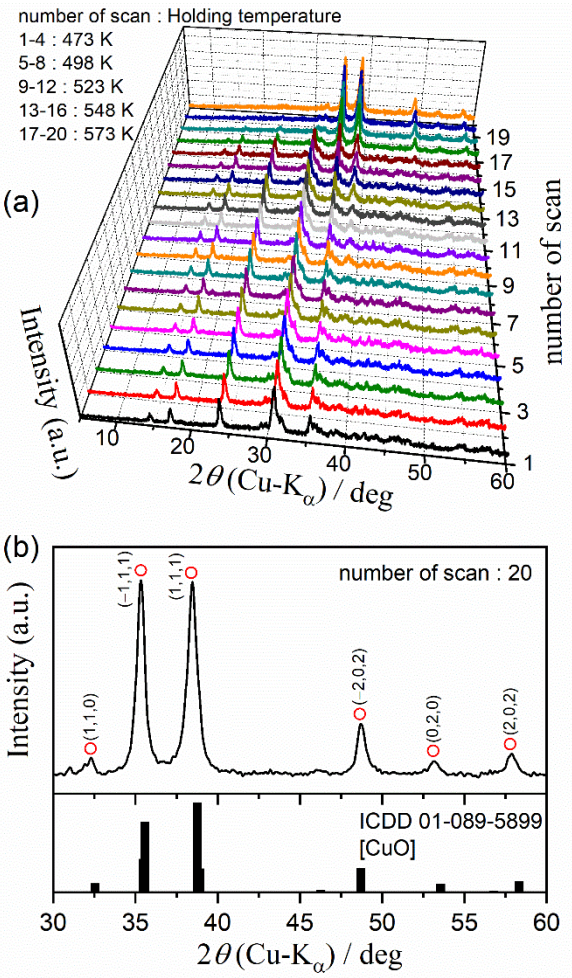

Figure S4. Changes in the XRD pattern during heating the granular malachite using a stepwise isothermal heating program with 60 min isothermal holding sections in a stream of CO_2 gas characterized by $p(CO_2)$ = 100 kPa (q_v = 100 cm^3 min^{-1}): (a) Changes in the XRD pattern with duration and temperature and (b) XRD pattern for the sample heated at 573 K for 45 min.

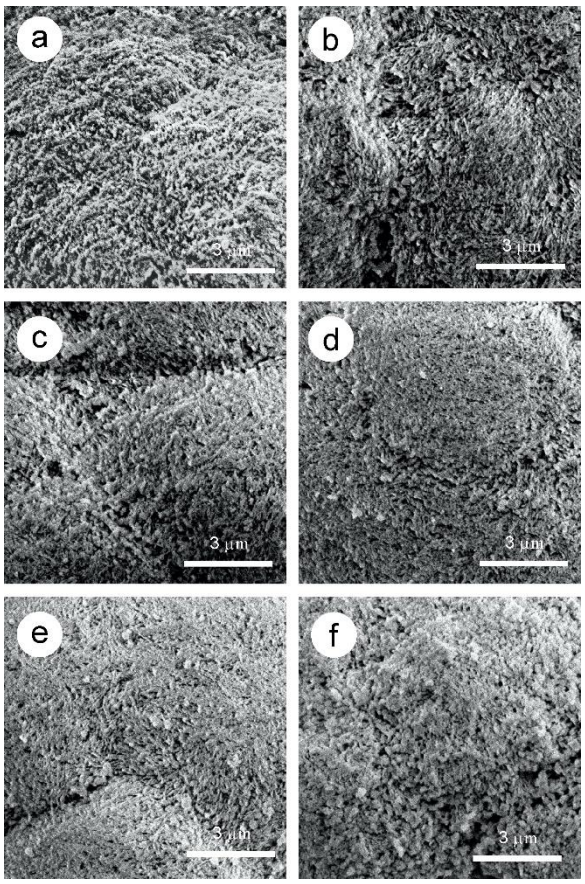

Figure S5. Surface morphologies of the granular particles heated to different temperatures at a β of 3 K min^{-1} in a stream of N_2–H_2O mixed gas ($p(H_2O)$ = 7.3 ± 0.1 kPa, q_v = 400 cm^3 min^{-1}): (a) T = 448 K (α = 0.01), (b) T = 466 K (α = 0.02), (c) T = 486 K (α = 0.07), (d) T = 506 K (α = 0.21), (e) T = 520 K (α = 0.50), and (f) T = 561 K (α = 0.97).

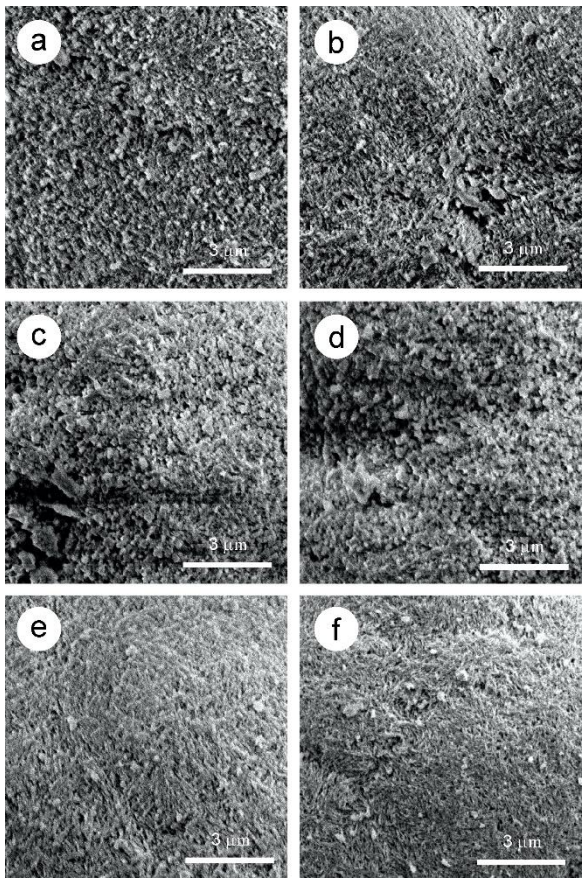

Figure S6. Surface morphologies of the granular particles heated to different temperatures at a β of 3 K min^{-1} in a stream of N_2–CO_2 mixed gas ($p(CO_2)$ = 19.9 ± 0.2 kPa, q_v = 300 cm^3 min^{-1}): (a) T = 457 K (α = 0.00), (b) T = 498 K (α = 0.02), (c) T = 531 K (α = 0.13), (d) T = 576 K (α = 0.36), (e) T = 583 K (α = 0.52), and (f) T = 619 K (α = 0.98).

S2. Effects of water vapor on the kinetics of thermal decomposition

S2-1. Formal kinetic analysis

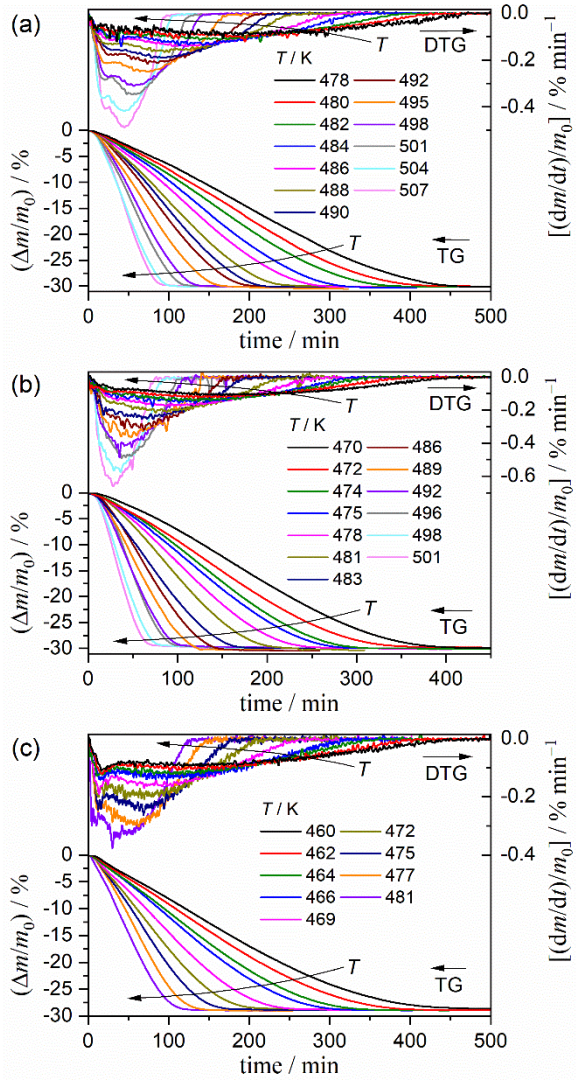

Figure S7. TG–DTG curves for the thermal decomposition of the granular malachite under isothermal conditions at different $p(H_2O)$ values: (a) $p(H_2O)$ = 1.0 ± 0.1 kPa (m_0 = 4.90 ± 0.13 mg), (b) $p(H_2O)$ = 3.0 ± 0.1 kPa (m_0 = 4.97 ± 0.11 mg), and (c) $p(H_2O)$ = 7.3 ± 0.1 kPa (m_0 = 4.98 ± 0.05 mg). Time zero was set when the mass-loss was started.

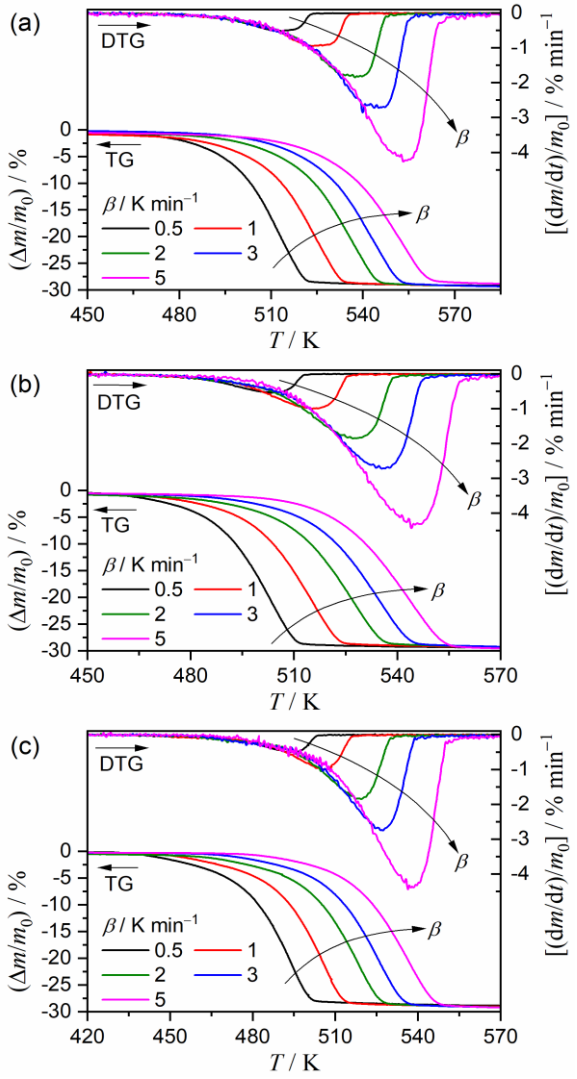

Figure S8. TG–DTG curves for the thermal decomposition of the granular malachite under linear nonisothermal conditions at different $p(H_2O)$ values: (a) $p(H_2O)$ = 0.9 ± 0.1 kPa (m_0 = 5.10 ± 0.10 mg), (b) $p(H_2O)$ = 2.8 ± 0.1 kPa (m_0 = 5.01 ± 0.11 mg), and (c) $p(H_2O)$ = 7.1 ± 0.2 kPa (m_0 = 5.02 ± 0.06 mg).

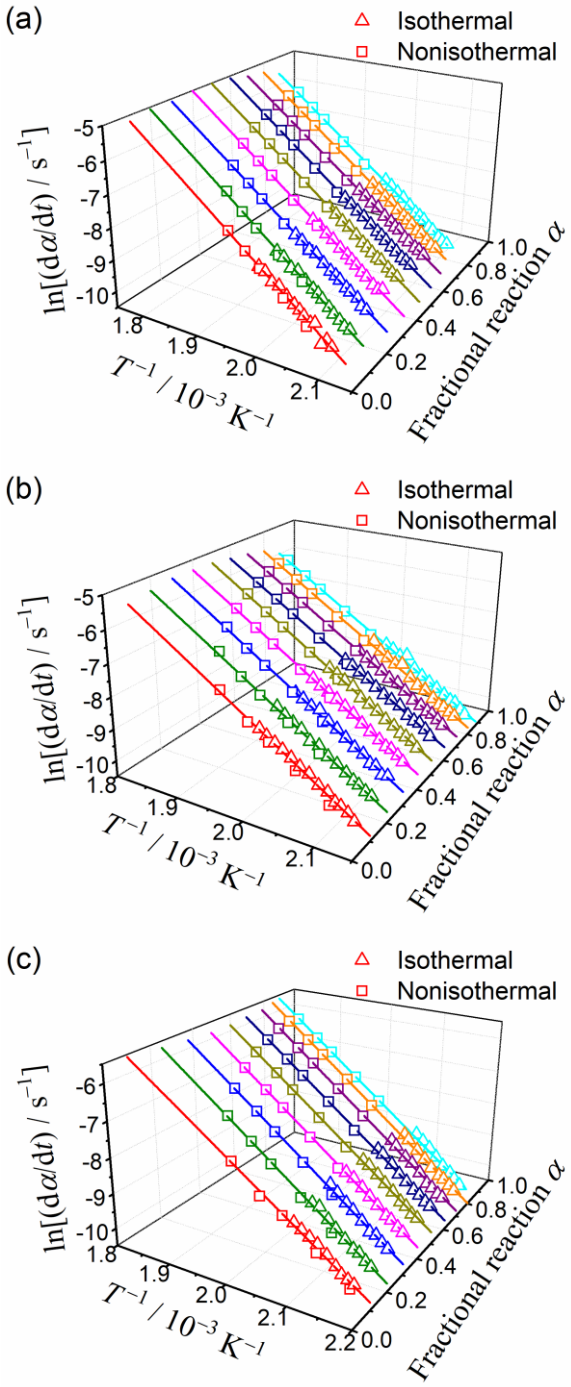

Figure S9. Friedman plots at different α for the thermal decomposition of granular malachite at different $p(H_2O)$ values: (a) $p(H_2O)$ = 0.9 kPa, (b) $p(H_2O)$ = 3.0 kPa, and (c) $p(H_2O)$ = 7.2 kPa.

S2-2. Mathematical deconvolution analysis

For the deconvolution of the DTG peak for the thermal decomposition of granular malachite under isothermal and linear nonisothermal conditions at various $p(H_2O)$, the Weibull function (eq. (S1)) was used for both reaction steps.

$$F(t) = a_0 \left(\frac{a_3 - 1}{a_3}\right)^{\frac{1-a_3}{a_3}} \left\{\frac{t - a_1}{a_2} + \left(\frac{a_3 - 1}{a_3}\right)^{\frac{1}{a_3}}\right\}^{a_3 - 1} \exp\left[-\left\{\frac{t - a_1}{a_2} + \left(\frac{a_3 - 1}{a_3}\right)^{\frac{1}{a_3}}\right\}^{a_3} + \frac{a_3 - 1}{a_3}\right], \quad \text{(S1)}$$

where a_0–a_3 are the amplitude, center, width, and shape, respectively. Figures S10–S12 show the typical results of the MDA under isothermal and linear nonisothermal conditions at $p(H_2O)$ of 0.9, 3.0, and 7.2 kPa, respectively. In all reactions at different $p(H_2O)$ values, statistically significant fits by two peaks were observed irrespective of the heating conditions. The contributions of first and second DTG peaks calculated by comparing the DTG peak areas separated by the MDA were invariant. The average value of contributions (c_1, c_2) is listed in Table S1.

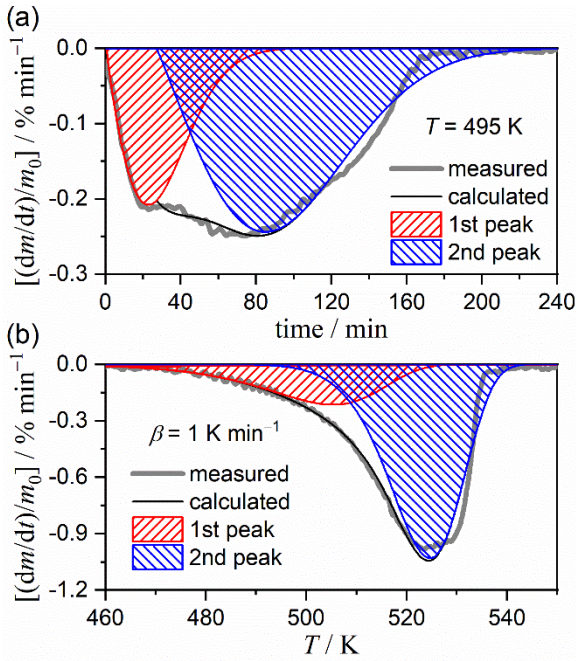

Figure S10. Typical results of MDA for the thermal decomposition of the granular malachite at $p(H_2O)$ = 0.9 kPa: (a) isothermal (T = 495 K) and (b) linear nonisothermal (β = 1 K min^{-1}) conditions.

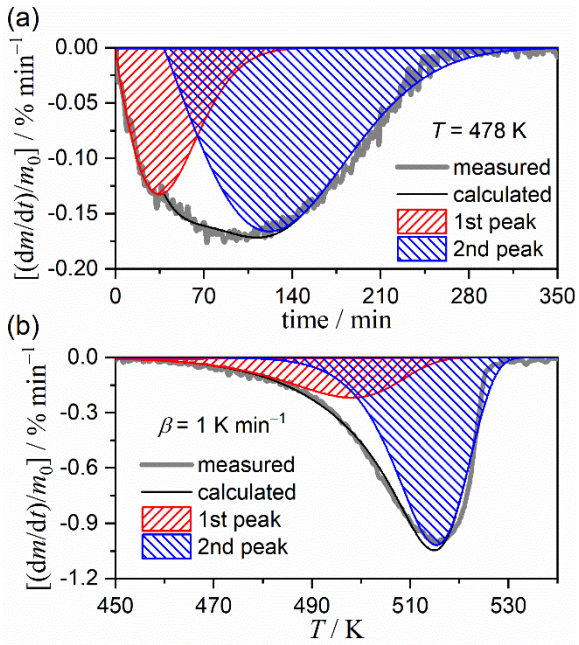

Figure S11. Typical results of MDA for the thermal decomposition of the granular malachite at $p(H_2O)$ = 3.0 kPa: (a) isothermal (T = 478 K) and (b) linear nonisothermal (β = 1 K min^{-1}) conditions.

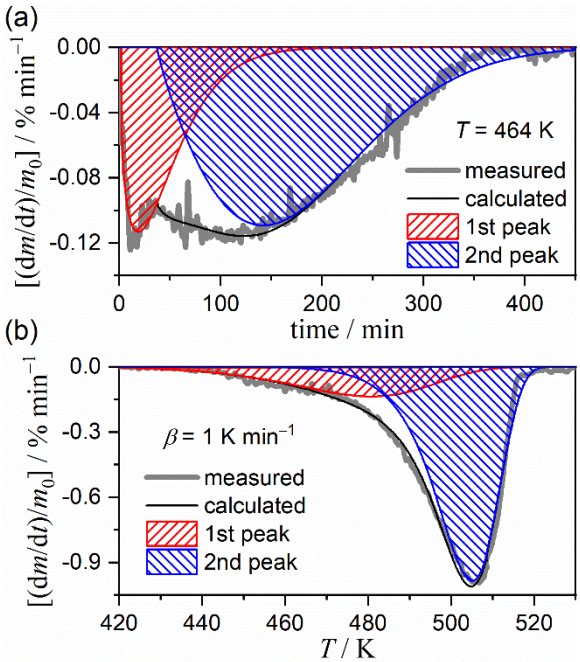

Figure S12. Typical results of MDA for the thermal decomposition of the granular malachite at $p(H_2O)$ = 7.2 kPa: (a) isothermal (T = 464 K) and (b) linear nonisothermal (β = 1 K min^{-1}) conditions.

Table S1. Kinetic parameters for the thermal decomposition of granular malachite at different $p(H_2O)$ values, determined from the MDA and subsequent formal kinetic analysis for each reaction step

$p(H_2O)$ / kPa	i	c_i	$E_{a,i}$ / kJ mol^{-1}, [a]	A_i / s^{-1}	$f_i(\alpha_i)=\alpha_i^{m(i)}(1-\alpha_i)^{n(i)}[-\ln(1-\alpha_i)]^{p(i)}$			R^2, [b]
					m_i	n_i	p_i	
0.9	1	0.26 ± 0.03	113.2 ± 4.9	(6.39 ± 0.17) × 10^8	−1.10 ± 0.20	1.27 ± 0.07	1.40 ± 0.19	0.9981
	2	0.74 ± 0.03	119.2 ± 1.6	(1.68 ± 0.01) × 10^9	0.30 ± 0.02	0.89 ± 0.01	0.24 ± 0.02	0.9999
3.0	1	0.26 ± 0.01	104.4 ± 4.4	(1.19 ± 0.03) × 10^8	−1.30 ± 0.19	1.33 ± 0.07	1.62 ± 0.18	0.9983
	2	0.74 ± 0.01	109.0 ± 3.1	(2.50 ± 0.01) × 10^8	0.06 ± 0.01	0.97 ± 0.01	0.48 ± 0.01	0.9999
7.2	1	0.25 ± 0.02	88.1 ± 5.8	(3.70 ± 0.03) × 10^6	−0.56 ± 0.06	1.14 ± 0.03	0.80 ± 0.06	0.9997
	2	0.75 ± 0.02	105.9 ± 4.7	(1.75 ± 0.01) × 10^8	0.16 ± 0.02	0.93 ± 0.01	0.36 ± 0.02	0.9999

[a] Average over $0.1 \leq \alpha_i \leq 0.9$

[b] Determination coefficient of the nonlinear least-squares analysis for the fitting of the kinetic curve using SB(m, n, p).

The mathematically separated DTG curves were used as the kinetic curves for each reaction step by normalizing using the fractional reactions (α_1, α_2) for the first and second reaction steps, respectively. Figures S13–S18 show the kinetic curves for each reaction step under isothermal (Figures S13, S15, and S17) and linear nonisothermal conditions (Figures S14, S16, and S18) at $p(H_2O)$ = 0.9 kPa (Figures S13 and S14), 3.0 kPa (Figures S15 and S16), and 7.2 kPa (Figures S17 and S18).

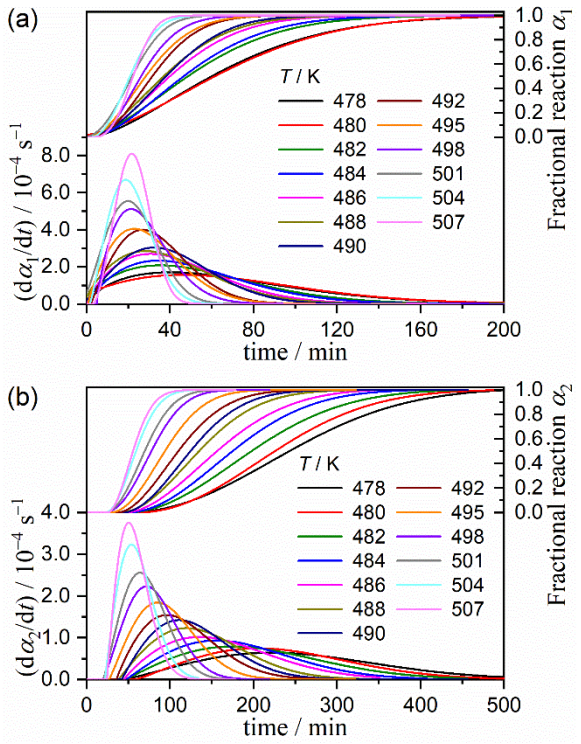

Figure S13. Kinetic curves for each component reaction step of the thermal decomposition of the granular malachite under isothermal conditions at $p(H_2O)$ = 0.9 kPa: (a) first and (b) second reaction steps.

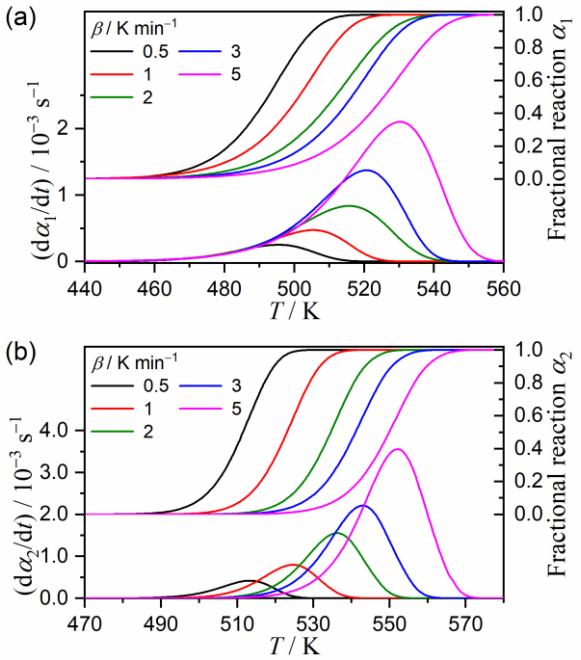

Figure S14. Kinetic curves for each component reaction step of the thermal decomposition of the granular malachite under linear nonisothermal conditions at $p(H_2O)$ = 0.9 kPa: (a) first and (b) second reaction steps.

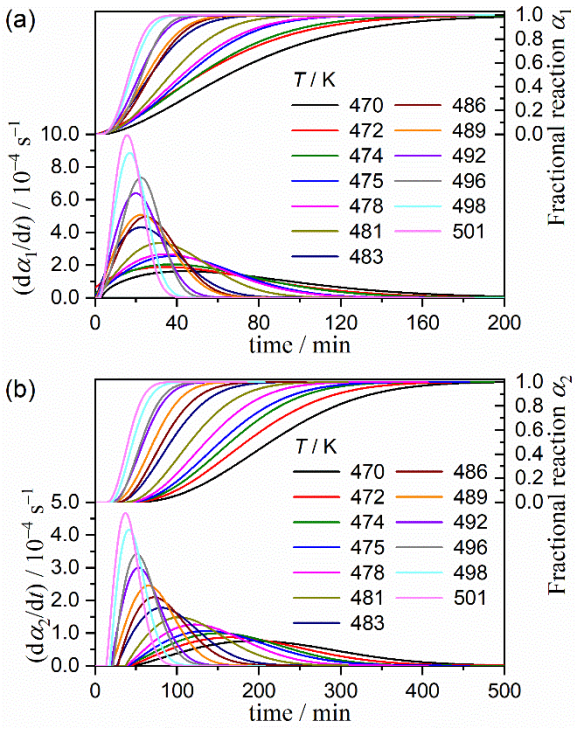

Figure S15. Kinetic curves for each component reaction step of the thermal decomposition of the granular malachite under isothermal conditions at $p(H_2O)$ = 3.0 kPa: (a) first and (b) second reaction steps.

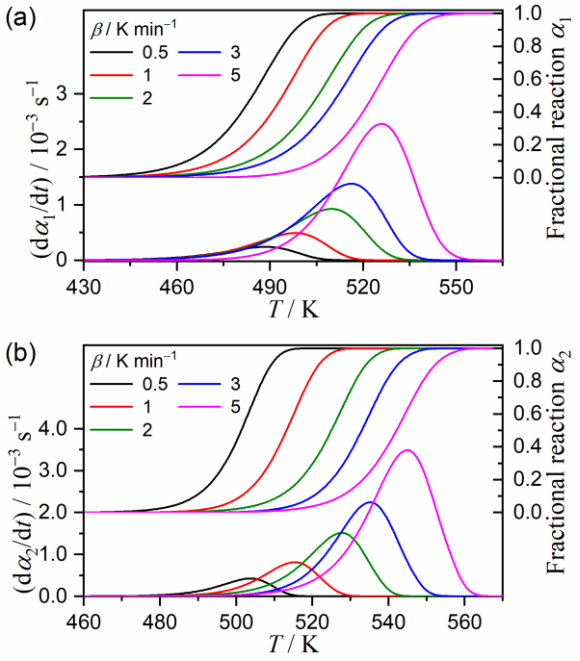

Figure S16. Kinetic curves for each component reaction step of the thermal decomposition of the granular malachite under linear nonisothermal conditions at $p(H_2O)$ = 3.0 kPa: (a) first and (b) second reaction steps.

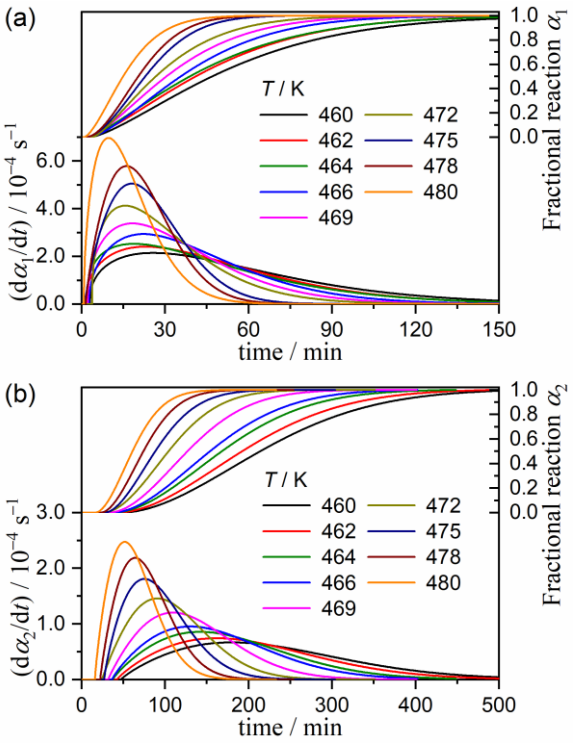

Figure S17. Kinetic curves for each component reaction step of the thermal decomposition of the granular malachite under isothermal conditions at $p(H_2O)$ = 7.2 kPa: (a) first and (b) second reaction steps.

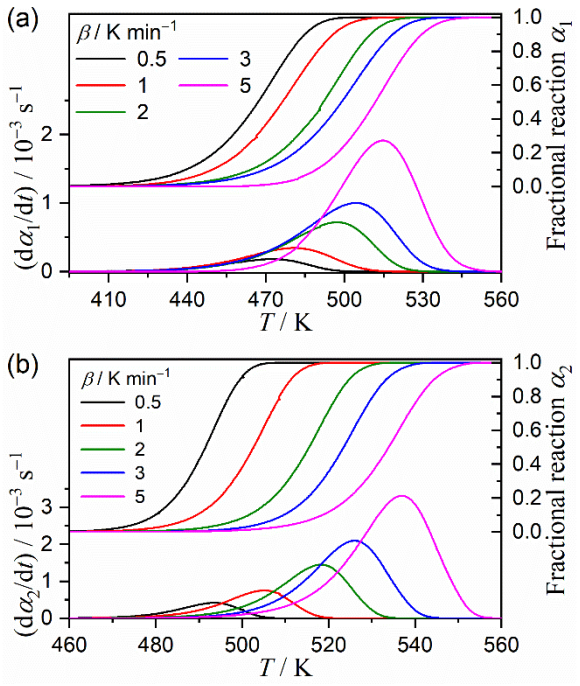

Figure S18. Kinetic curves for each component reaction step of the thermal decomposition of the granular malachite under linear nonisothermal conditions at $p(H_2O)$ = 7.2 kPa: (a) first and (b) second reaction steps.

The kinetic curves for each reaction step at each $p(H_2O)$ value were subjected to the Friedman plots. Figures S19–S21 show the Friedman plots at various α_i values at $p(H_2O)$ = 0.9, 3.0, and 7.2 kPa, respectively. Irrespective of the reaction step, the Friedman plots involving the data points under isothermal and linear nonisothermal conditions showed a statistically significant linear correlation at α_i values over a wide range. This was observed irrespective of $p(H_2O)$. Figures S22–S24 show the $E_{a,i}$ values at different α_i values and the experimental master plots for the first and second reaction steps at different $p(H_2O)$ values of 0.9, 3.0, and 7.2 kPa, respectively. The $E_{a,i}$ values were relatively constant during each reaction step. The $E_{a,2}$ values were slightly larger than the $E_{a,1}$ values, particularly in the second half of each reaction step (Figures S22(a), S23(a), and S24(a)). Table S1 lists the average $E_{a,i}$ values in a range of $0.1 \le \alpha_i \le 0.9$. In both first and second reaction steps, $E_{a,i}$ decreased with increasing $p(H_2O)$. Using the average $E_{a,i}$ values, the experimental master plots were generated by calculating the hypothetical reaction rate ($d\alpha_i/d\theta_i$) at an infinite temperature at each α_i value according to eq. (S2).[10, 51-54]

$$\frac{d\alpha_i}{d\theta_i} = \left(\frac{d\alpha_i}{dt}\right)\exp\left(\frac{E_{a,i}}{RT}\right) = A_i f_i(\alpha_i) \qquad \text{with} \qquad \theta_i = \int_0^t \exp\left(-\frac{E_{a,i}}{RT}\right)dt \qquad \text{(S2)}$$

where θ is Ozawa's generalized time[55,56] denoting the hypothetical reaction time at infinite temperature. Plots of ($d\alpha_i/d\theta_i$) versus α_i for both reaction steps at all $p(H_2O)$ exhibited a maximum reaction rate midway through the reaction step. A distinguishable variation by the effect of $p(H_2O)$ was observed for the initial reaction stage of the first reaction step where an initial deceleration part decreased with increasing $p(H_2O)$. The experimental master plots were fitted using the SB(m_i, n_i, p_i) model (eq. (6)) by optimizing the A_i value and the kinetic exponents in SB(m_i, n_i, p_i). Table S1 lists the optimized A_i and the kinetic exponents. The kinetic parameters including (c_1, c_2) values obtained by the MDA and subsequent formal kinetic analysis for each reaction step at a certain $p(H_2O)$ value were used as the initial values for additional optimization via KDA.

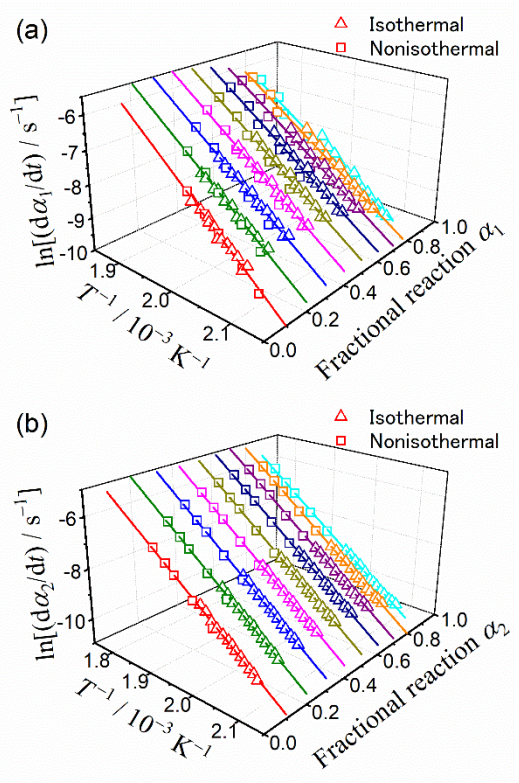

Figure S19. Friedman plots for each reaction step of the thermal decomposition of the granular malachite at $p(H_2O)$ = 0.9 kPa: (a) first and (b) second reaction steps.

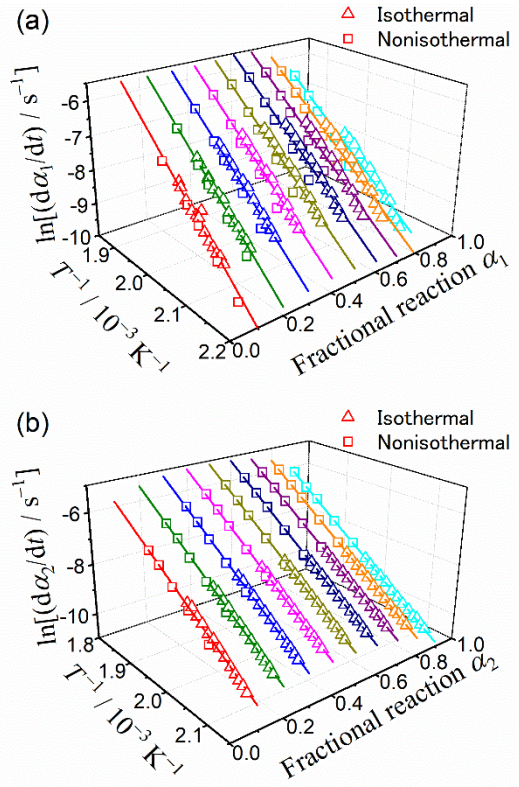

Figure S20. Friedman plots for each reaction step of the thermal decomposition of the granular malachite at $p(H_2O)$ = 3.0 kPa: (a) first and (b) second reaction steps.

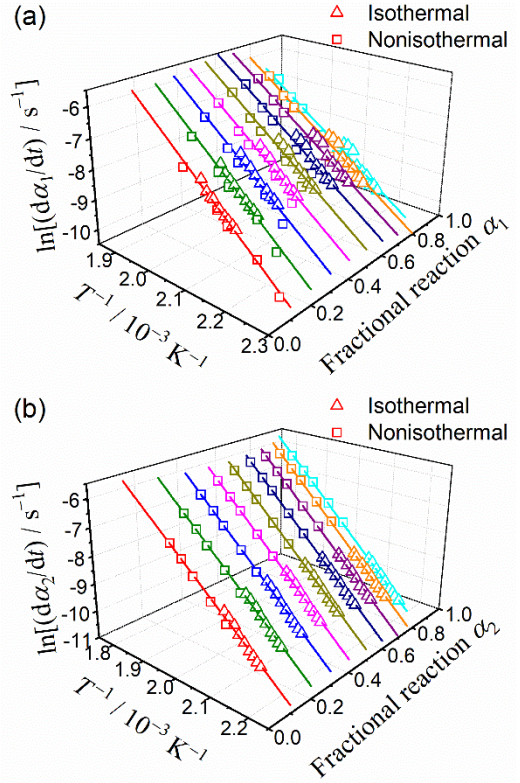

Figure S21. Friedman plots for each reaction step of the thermal decomposition of the granular malachite at $p(H_2O)$ = 7.2 kPa: (a) first and (b) second reaction steps.

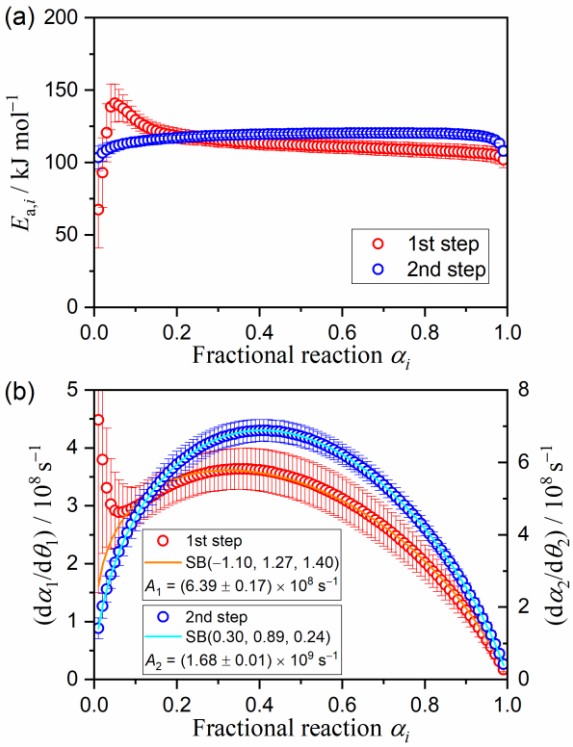

Figure S22. Kinetic results for each reaction step of the thermal decomposition of the granular malachite at $p(H_2O)$ = 0.9 kPa: (a) $E_{a,i}$ values at different α_i and (b) experimental master plots of ($d\alpha_i/d\theta_i$) versus α_i.

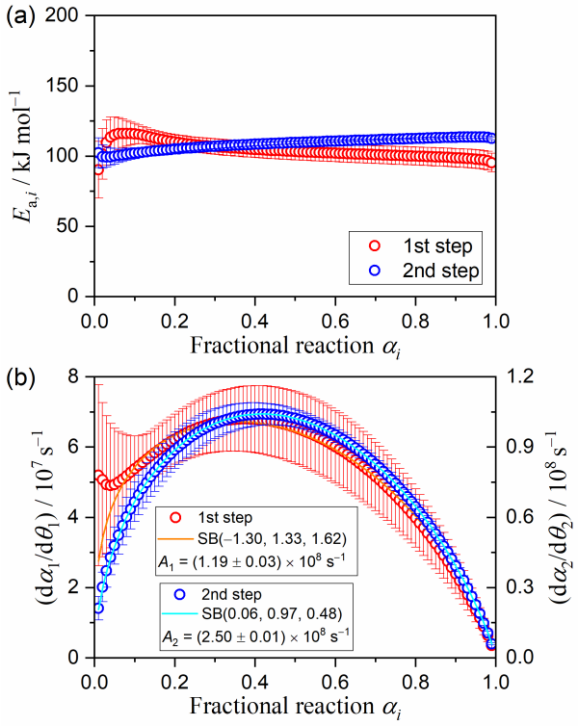

Figure S23. Kinetic results for each reaction step of the thermal decomposition of the granular malachite at $p(H_2O)$ = 3.0 kPa: (a) $E_{a,i}$ values at different α_i and (b) experimental master plots of ($d\alpha_i/d\theta_i$) versus α_i.

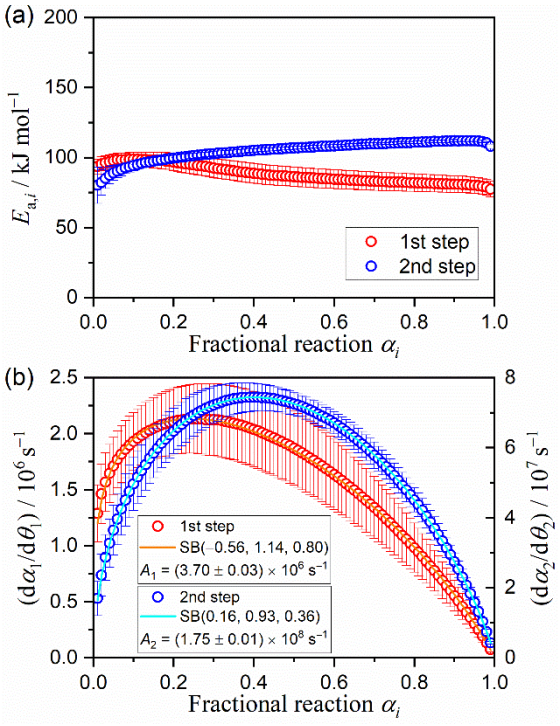

Figure S24. Kinetic results for each reaction step of the thermal decomposition of the granular malachite at $p(H_2O)$ = 7.2 kPa: (a) $E_{a,i}$ values at different α_i and (b) experimental master plots of ($d\alpha_i/d\theta_i$) versus α_i.

S2-3. Kinetic deconvolution analysis

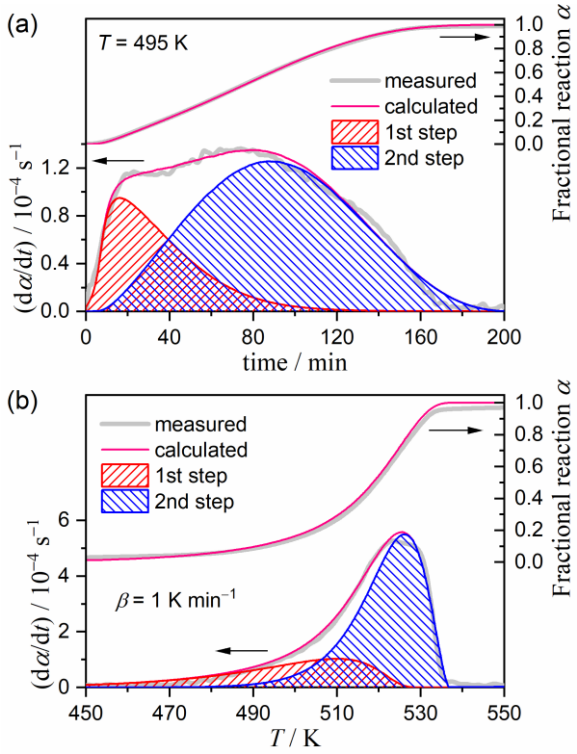

Figure S25. Typical results of KDA for the thermal decomposition of the granular malachite at $p(H_2O)$ = 0.9 kPa: (a) isothermal (T = 495 K) and (b) linear nonisothermal (β = 1 K min^{-1}) conditions.

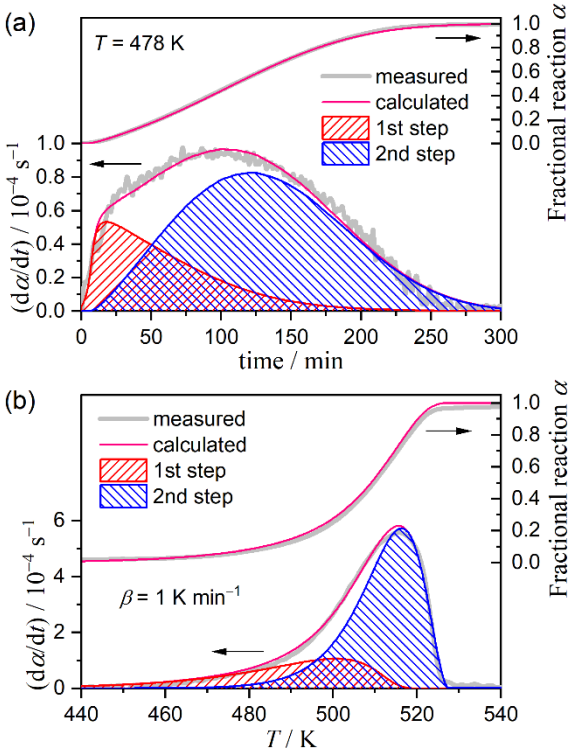

Figure S26. Typical results of KDA for the thermal decomposition of the granular malachite at $p(H_2O)$ = 3.0 kPa: (a) isothermal (T = 478 K) and (b) linear nonisothermal (β = 1 K min^{-1}) conditions.

Table S2. Optimized kinetic parameters via KDA for the thermal decomposition of the granular malachite under isothermal conditions

$p(H_2O)$ / kPa	i	c_i	$E_{a,i}$ / kJ mol^{-1}	A_i / s^{-1}	$f_i(\alpha_i)=\alpha_i^{m(i)}(1-\alpha_i)^{n(i)}[-\ln(1-\alpha_i)]^{p(i)}$			$R^{2,a}$
					m_i	n_i	p_i	
0.9	1	0.26 ± 0.01	114.7 ± 0.2	(6.39 ± 0.01) × 10^8	−1.16 ± 0.01	1.32 ± 0.01	1.28 ± 0.01	0.9930 ± 0.0070
	2	0.74 ± 0.01	119.8 ± 0.1	(1.68 ± 0.01) × 10^9	0.32 ± 0.01	0.76 ± 0.01	0.26 ± 0.01	
3.0	1	0.26 ± 0.01	106.1 ± 0.8	(1.19 ± 0.01) × 10^8	−1.36 ± 0.05	1.33 ± 0.07	1.50 ± 0.06	0.9941 ± 0.0030
	2	0.74 ± 0.01	109.6 ± 0.3	(2.49 ± 0.01) × 10^8	0.06 ± 0.01	0.86 ± 0.09	0.50 ± 0.02	
7.2	1	0.24 ± 0.01	88.9 ± 0.3	(3.70 ± 0.01) × 10^6	−0.58 ± 0.01	1.18 ± 0.01	0.75 ± 0.01	0.9925 ± 0.0032
	2	0.76 ± 0.01	106.1 ± 0.3	(1.75 ± 0.01) × 10^8	0.16 ± 0.01	0.86 ± 0.02	0.39 ± 0.01	

[a] Determination coefficient of the nonlinear least-squares analysis.

Table S3. Optimized kinetic parameters via KDA for the thermal decomposition of the granular malachite under linear nonisothermal conditions

$p(H_2O)$ / kPa	i	c_i	$E_{a,i}$ / kJ mol^{-1}	A_i / s^{-1}	$f_i(\alpha_i)=\alpha_i^{m(i)}(1-\alpha_i)^{n(i)}[-\ln(1-\alpha_i)]^{p(i)}$			$R^{2,a}$
					m_i	n_i	p_i	
0.9	1	0.28 ± 0.02	117.1 ± 0.8	(6.91 ± 1.23) × 10^8	−1.59 ± 0.04	1.07 ± 0.02	1.43 ± 0.03	0.9999 ± 0.0001
	2	0.72 ± 0.02	119.8 ± 0.7	(1.58 ± 0.18) × 10^9	0.31 ± 0.01	0.71 ± 0.05	0.26 ± 0.01	
3.0	1	0.27 ± 0.01	107.4 ± 0.7	(1.19 ± 0.01) × 10^8	−1.54 ± 0.05	1.07 ± 0.01	1.49 ± 0.06	0.9996 ± 0.0006
	2	0.73 ± 0.01	109.7 ± 0.2	(2.38 ± 0.01) × 10^8	0.06 ± 0.01	0.79 ± 0.03	0.50 ± 0.02	
7.2	1	0.24 ± 0.01	88.8 ± 0.4	(3.62 ± 0.11) × 10^6	−0.59 ± 0.03	1.12 ± 0.08	0.75 ± 0.04	0.9999 ± 0.0001
	2	0.76 ± 0.01	106.6 ± 0.3	(1.76 ± 0.01) × 10^8	0.16 ± 0.01	0.77 ± 0.06	0.38 ± 0.03	

[a] Determination coefficient of the nonlinear least-squares analysis.

S2-4. Universal kinetic analysis over different $p(H_2O)$ values

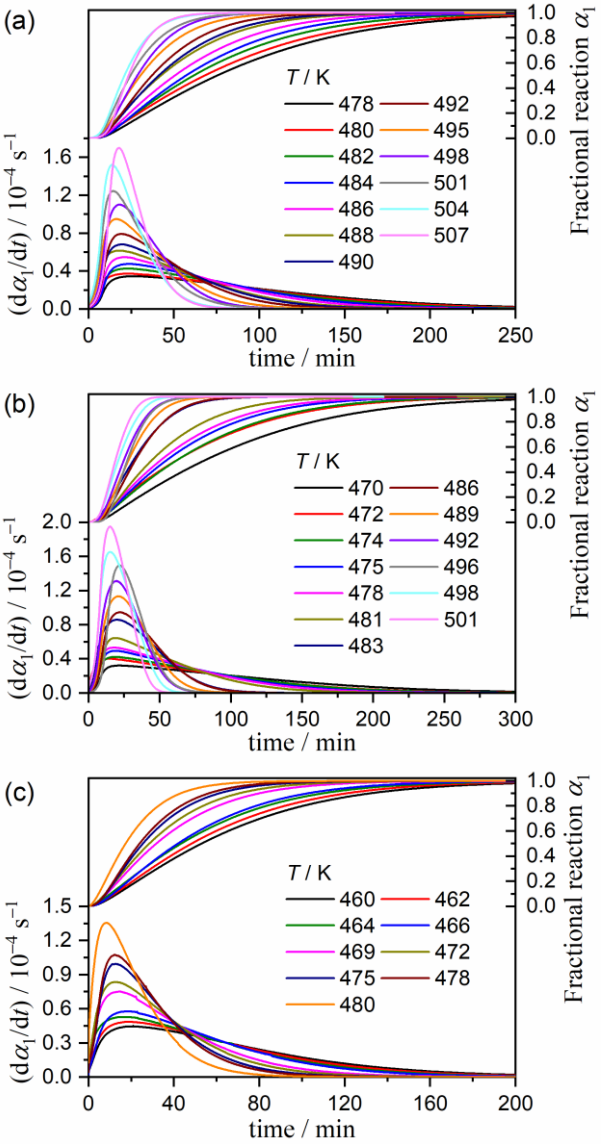

Figure S27. Kinetic curves for the first reaction step of the thermal decomposition of the granular malachite under isothermal conditions at each $p(H_2O)$: (a) 0.9, (b) 3.0, and (c) 7.2 kPa.

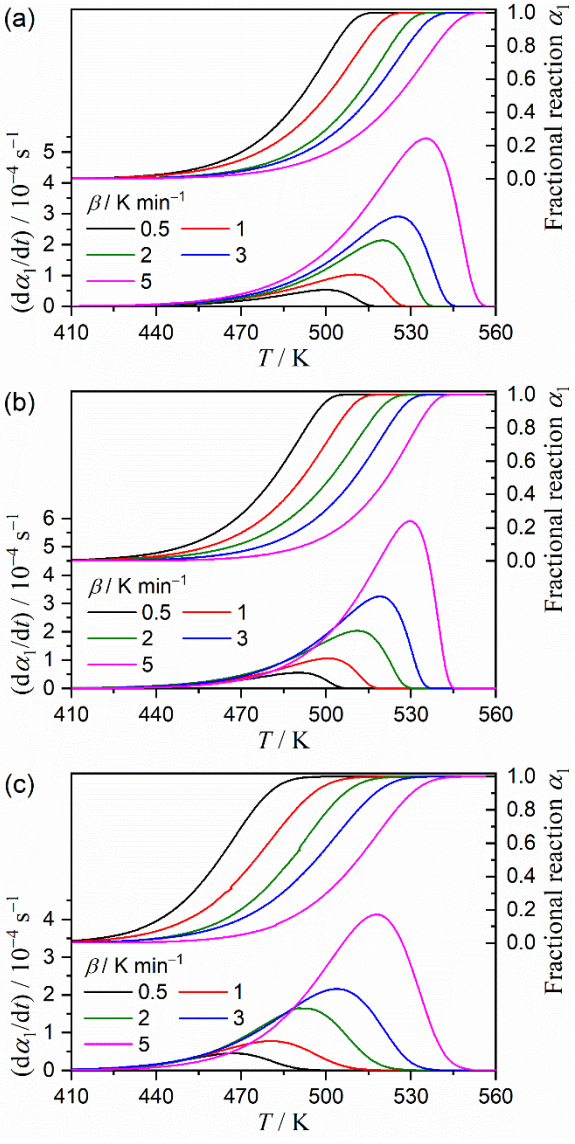

Figure S28. Kinetic curves for the first reaction step of the thermal decomposition of the granular malachite under linear nonisothermal conditions at each $p(H_2O)$: (a) 0.9, (b) 3.0, and (c) 7.2 kPa.

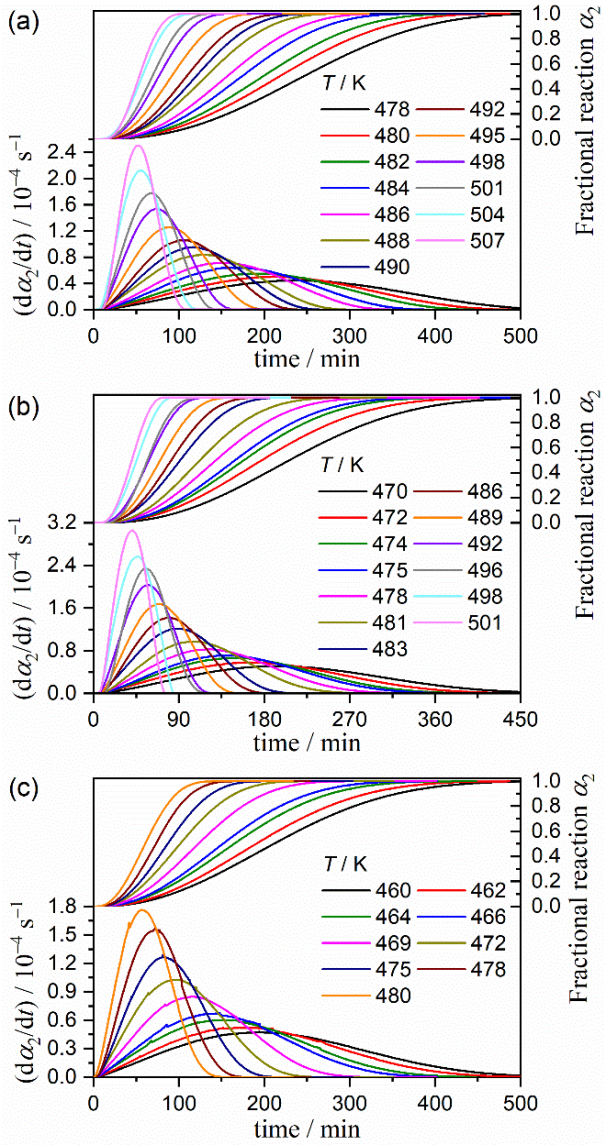

Figure S29. Kinetic curves for the second reaction step of the thermal decomposition of the granular malachite under isothermal conditions at each $p(H_2O)$: (a) 0.9, (b) 3.0, and (c) 7.2 kPa.

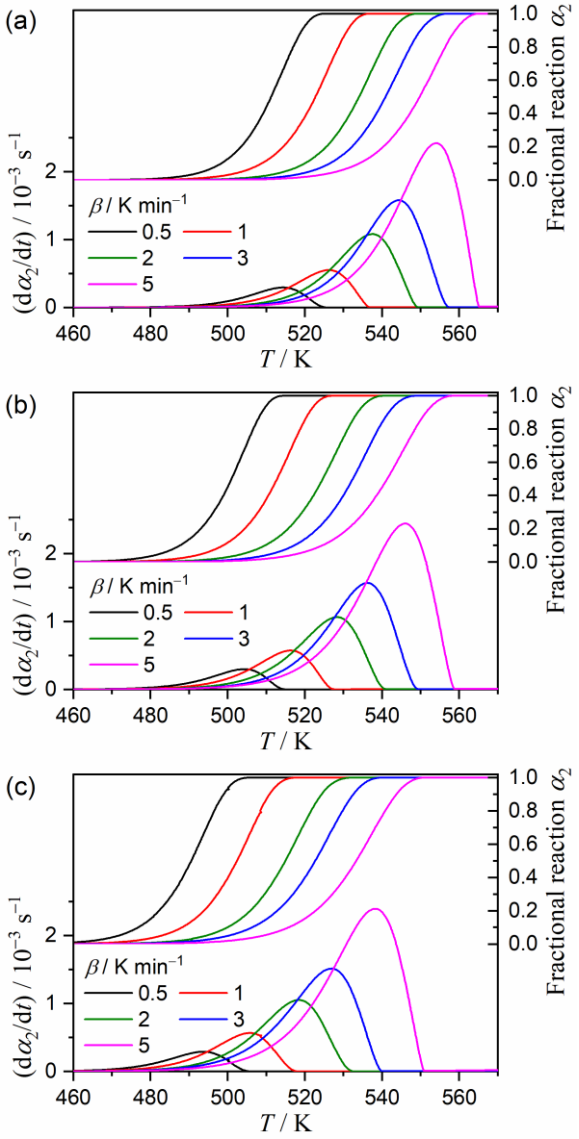

Figure S30. Kinetic curves for the second reaction step of the thermal decomposition of the granular malachite under linear nonisothermal conditions at each $p(H_2O)$: (a) 0.9, (b) 3.0, and (c) 7.2 kPa.

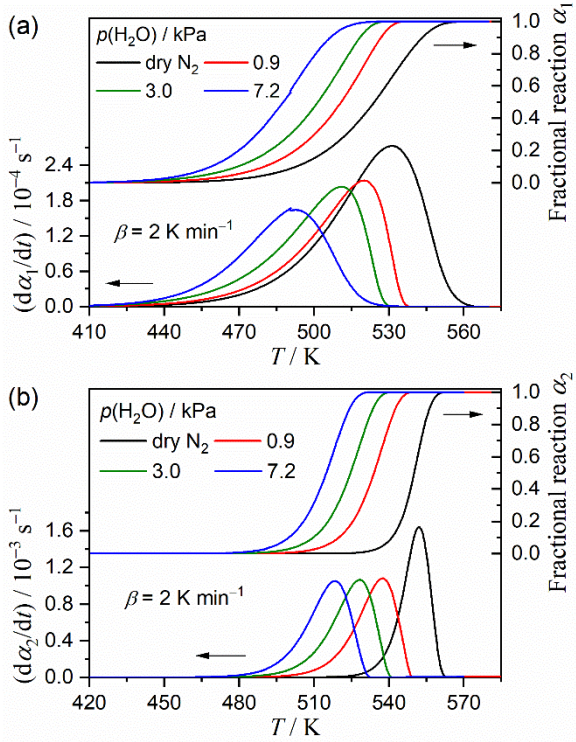

Figure S31. Comparison of the kinetic curves of each reaction step of the thermal decomposition of granular malachite under linear nonisothermal conditions at a β of 2 K min^{-1} under different $p(H_2O)$ values: (a) first and (b) second reaction steps.

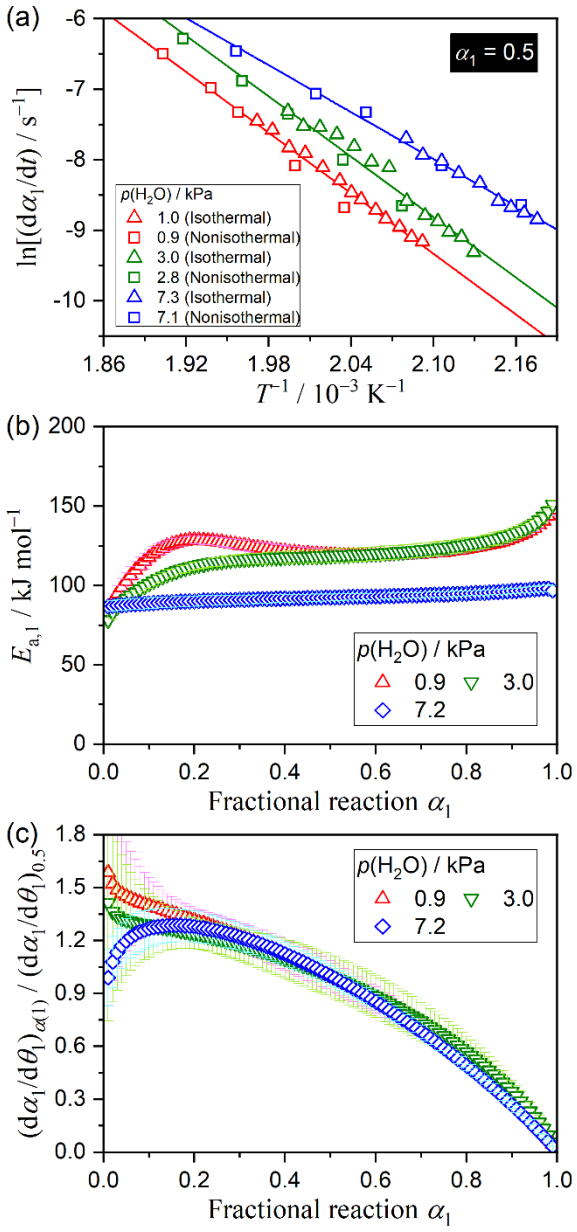

Figure S32. Formal kinetic analysis for the first reaction step of the thermal decomposition of the granular malachite under different $p(H_2O)$: (a) Friedman plots at $\alpha_1 = 0.5$, (b) $E_{a,1}$ values at different α_1 values, and (c) experimental master plots of $(d\alpha_1/d\theta_1)_{\alpha(1)}/(d\alpha_1/d\theta_1)_{0.5}$ versus α_1.

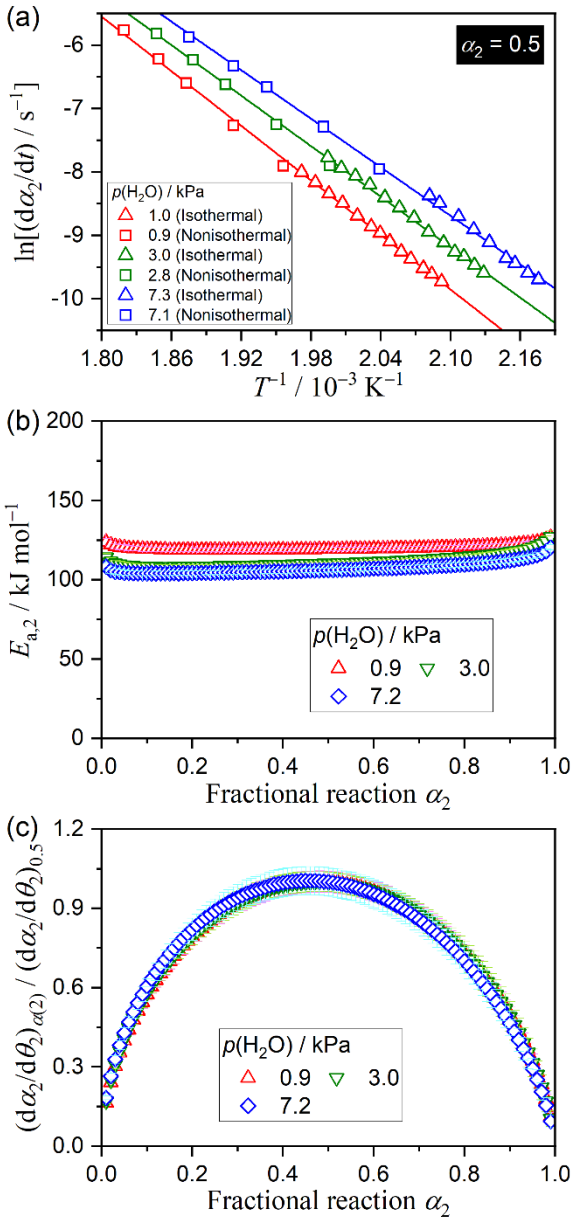

Figure S33. Formal kinetic analysis for the second reaction step of the thermal decomposition of the granular malachite under different $p(H_2O)$: (a) Friedman plots at $\alpha_2 = 0.5$, (b) $E_{a,2}$ values at different α_2 values, and (c) experimental master plots of $(d\alpha_2/d\theta_2)_{\alpha(2)}/(d\alpha_2/d\theta_2)_{0.5}$ versus α_2.

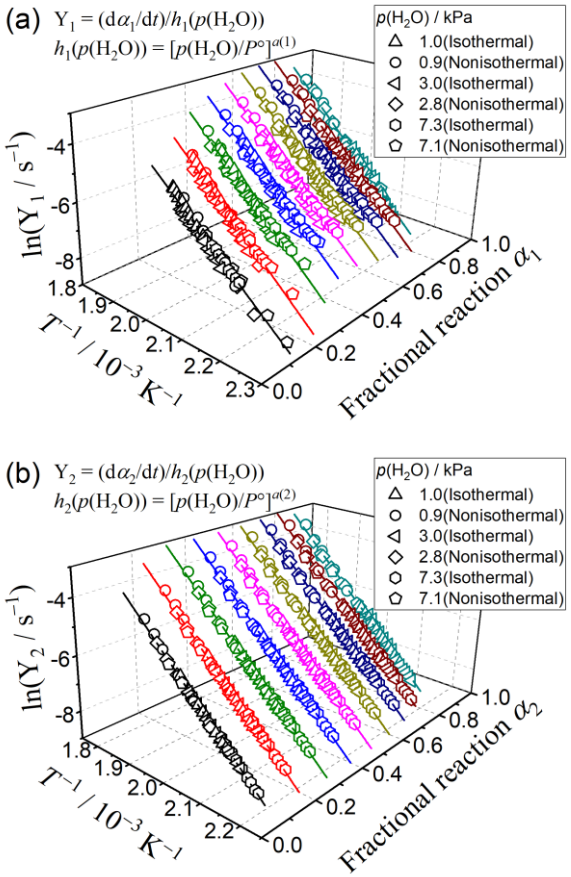

Figure S34. Extended Friedman plots over different $p(H_2O)$ for each reaction step of the thermal decomposition of the granular malachite: (a) first and (b) second reaction steps.

S3. Effects of CO_2 on the kinetics of thermal decomposition

S3-1. Formal kinetic analysis

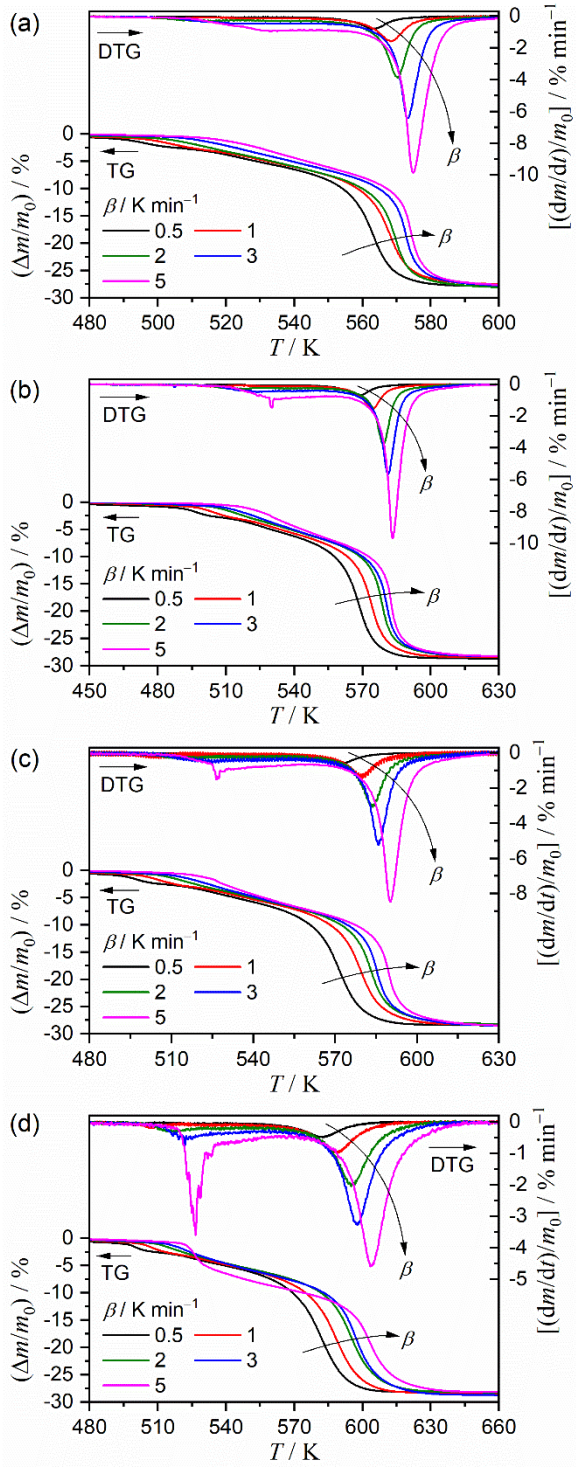

Figure S35. TG–DTG curves for the thermal decomposition of the granular malachite under linear nonisothermal conditions at various β values at different $p(CO_2)$: (a) $p(CO_2)$ = 4.9 ± 0.1 kPa (m_0 = 5.06 ± 0.14 mg), (b) $p(CO_2)$ = 10.0 ± 0.2 kPa (m_0 = 5.00 ± 0.05 mg), (c) $p(CO_2)$ = 20.0 ± 0.1 kPa (m_0 = 5.00 ± 0.03 mg), and (d) $p(CO_2)$ = 100 kPa (m_0 = 5.01 ± 0.03 mg).

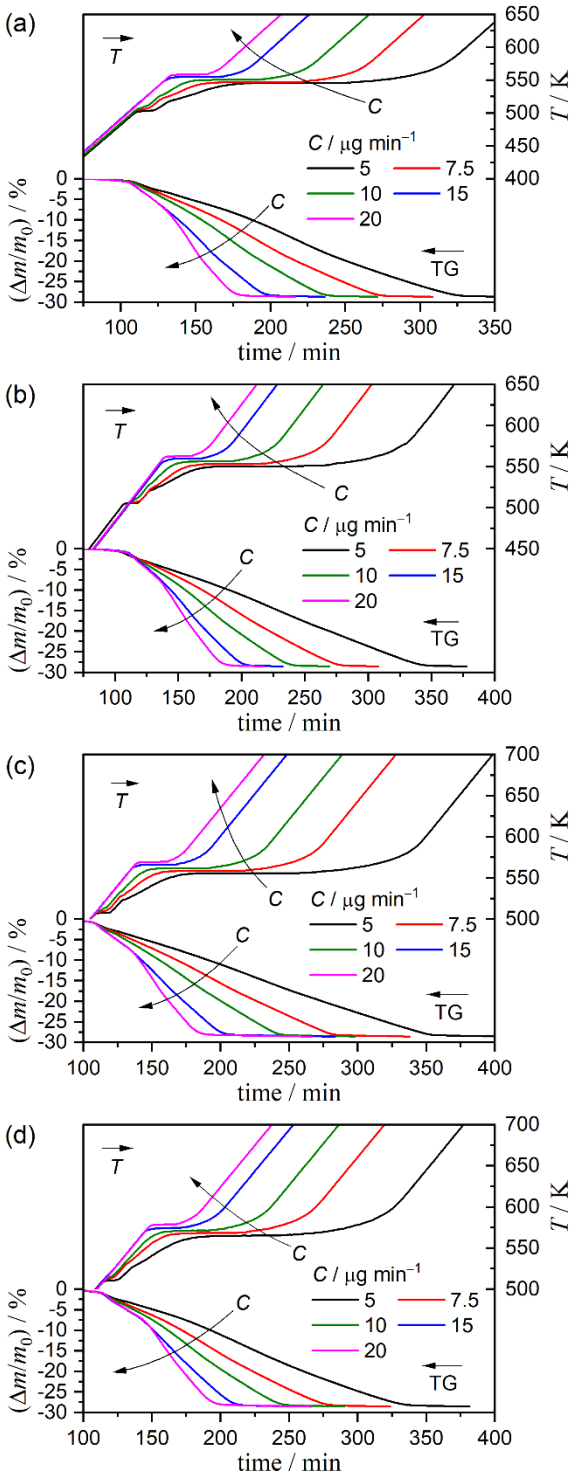

Figure S36. TG and temperature profile curves for the thermal decomposition of the granular malachite under stepwise isothermal conditions at various C values at different $p(CO_2)$: (a) $p(CO_2)$ = 5.0 ± 0.1 kPa (m_0 = 4.99 ± 0.02 mg), (b) $p(CO_2)$ = 9.9 ± 0.3 kPa (m_0 = 5.00 ± 0.02 mg), (c) $p(CO_2)$ = 20.0 ± 0.1 kPa (m_0 = 5.00 ± 0.03 mg), and (d) $p(CO_2)$ = 100 kPa (m_0 = 5.00 ± 0.03 mg).

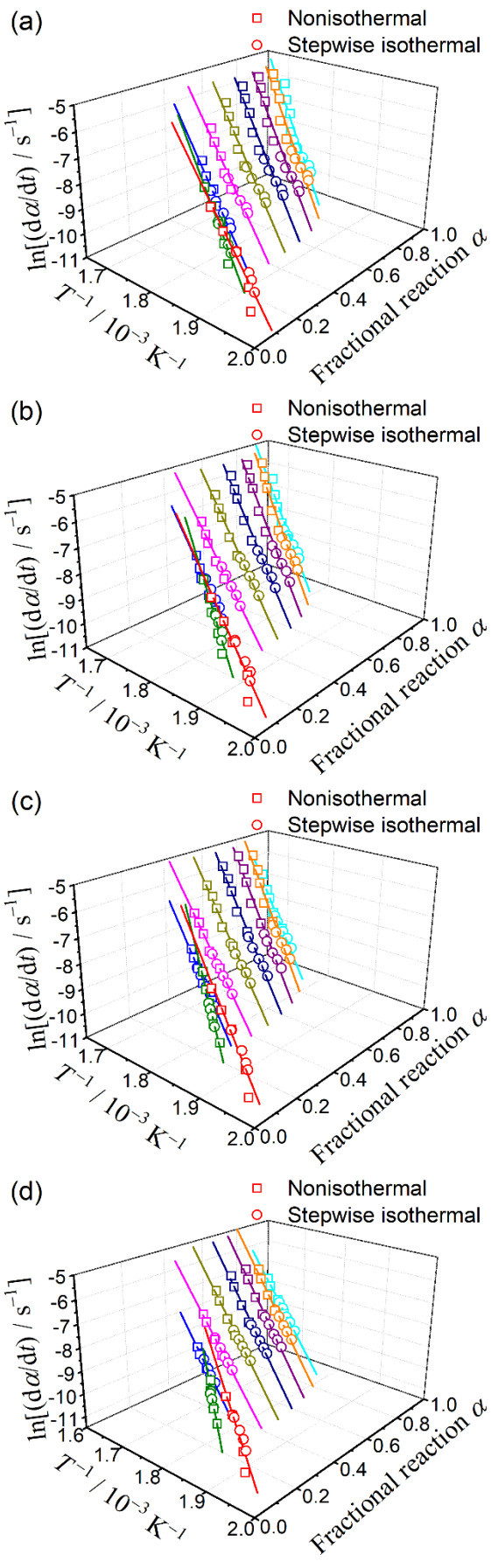

Figure S37. Friedman plots at different α for the thermal decomposition of the granular malachite at different $p(CO_2)$ values: (a) 5.0, (b) 10.0, (c) 20.0, and (d) 100 kPa.

S3-2. Mathematical deconvolution analysis

Figure S38 shows the typical results of MDA using the Weibull functions for the DTG curves of the thermal decomposition of the granular malachite at different $p(CO_2)$ values. Table S4 lists the contributions of each reaction step to the overall thermal decomposition estimated by the MDA as the average value over reactions at different β values. Figures S39–S42 show the kinetic curves of each reaction step at different β values for the reactions at different $p(CO_2)$ values of 5.0, 10.0, 20.0, and 100 kPa, respectively.

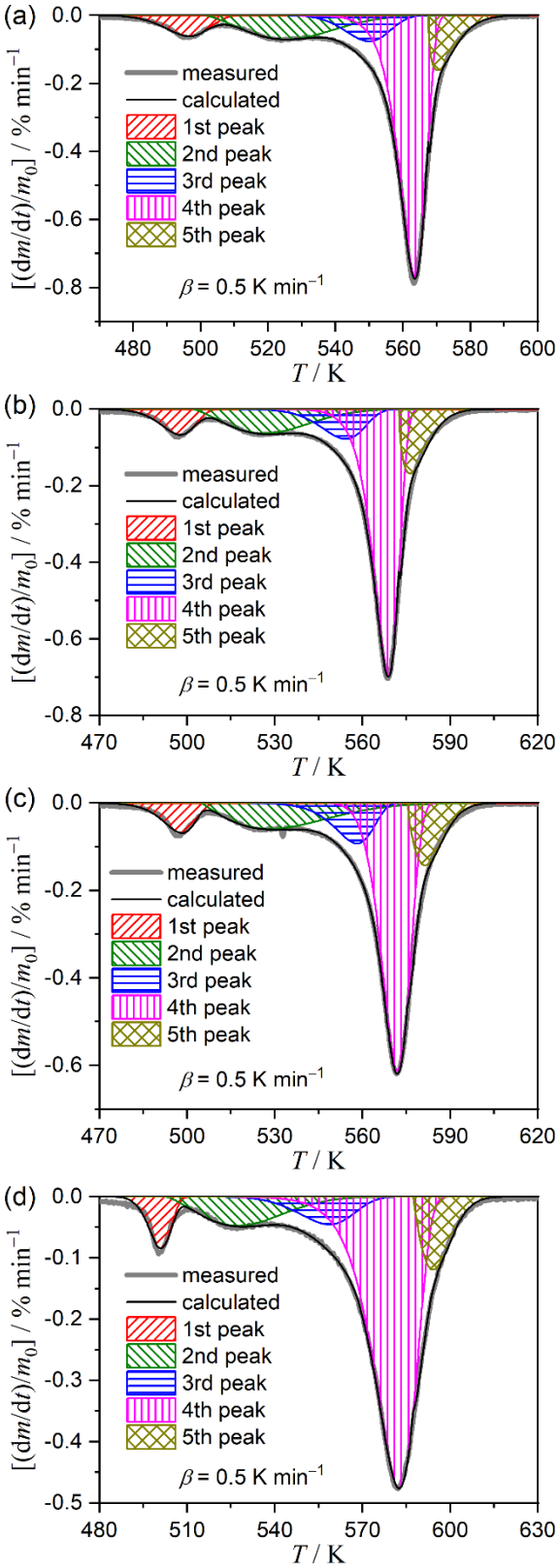

Figure S38. Typical results of MDA using Weibull functions for the DTG curves of the thermal decomposition of the granular malachite at a β of 0.5 K min^{-1} at different $p(CO_2)$ values: (a) 5.0, (b) 10.0, (c) 20.0, and (d) 100 kPa.

Table S4. Kinetic parameters for the thermal decomposition of the granular malachite at different $p(CO_2)$ values, determined by the MDA and subsequent formal kinetic analysis for each reaction step

$p(CO_2)$ / kPa	i	c_i	$E_{a,i}$ / kJ mol^{-1}, [a]	A_i / s^{-1}	$f_i(\alpha_i)=\alpha_i^{m(i)}(1-\alpha_i)^{n(i)}[-\ln(1-\alpha_i)]^{p(i)}$			R^2, [b]
					m_i	n_i	p_i	
5.0	1	0.10 ± 0.02	142.2 ± 4.1	(1.39 ± 0.01) × 10^{12}	0.45 ± 0.03	0.91 ± 0.01	0.04 ± 0.03	0.9999
	2	0.16 ± 0.02	313.7 ± 28.7	(1.86 ± 0.05) × 10^{28}	4.26 ± 0.22	0.26 ± 0.08	–4.18 ± 0.21	0.9984
	3	0.12 ± 0.04	396.9 ± 4.6	(8.32 ± 0.12) × 10^{34}	2.19 ± 0.13	0.50 ± 0.05	–1.96 ± 0.13	0.9992
	4	0.54 ± 0.05	566.2 ± 58.0	(7.90 ± 0.01) × 10^{49}	0.37 ± 0.09	0.98 ± 0.04	0.09 ± 0.09	0.9983
	5	0.09 ± 0.02	489.3 ± 13.4	(1.21 ± 0.02) × 10^{42}	1.78 ± 0.07	1.10 ± 0.03	–1.65 ± 0.07	0.9998
10.0	1	0.10 ± 0.04	126.8 ± 3.7	(3.33 ± 0.01) × 10^{10}	0.09 ± 0.01	0.99 ± 0.01	0.48 ± 0.01	0.9999
	2	0.14 ± 0.02	256.0 ± 19.8	(3.20 ± 0.07) × 10^{22}	3.40 ± 0.15	0.56 ± 0.05	–3.23 ± 0.14	0.9986
	3	0.20 ± 0.07	226.0 ± 3.0	(2.33 ± 0.03) × 10^{18}	0.58 ± 0.10	0.91 ± 0.04	–0.25 ± 0.09	0.9996
	4	0.45 ± 0.07	493.1 ± 58.3	(3.81 ± 0.05) × 10^{42}	–0.54 ± 0.08	1.21 ± 0.03	1.00 ± 0.08	0.9997
	5	0.11 ± 0.02	358.1 ± 65.4	(5.69 ± 0.05) × 10^{29}	1.56 ± 0.07	1.02 ± 0.03	–1.43 ± 0.07	0.9998
20.0	1	0.10 ± 0.03	146.5 ± 2.9	(3.56 ± 0.01) × 10^{12}	0.17 ± 0.01	0.97 ± 0.01	0.37 ± 0.01	0.9999
	2	0.16 ± 0.02	416.4 ± 88.0	(1.27 ± 0.05) × 10^{38}	8.68 ± 0.38	–0.56 ± 0.14	–8.85 ± 0.37	0.9969
	3	0.13 ± 0.03	272.9 ± 11.9	(4.33 ± 0.02) × 10^{22}	0.32 ± 0.03	0.90 ± 0.01	–0.07 ± 0.03	0.9999
	4	0.49 ± 0.03	419.1 ± 50.5	(3.19 ± 0.02) × 10^{35}	–0.23 ± 0.05	1.12 ± 0.02	0.70 ± 0.05	0.9998
	5	0.12 ± 0.01	340.4 ± 56.6	(6.82 ± 0.04) × 10^{27}	1.67 ± 0.05	0.97 ± 0.02	–1.53 ± 0.05	0.9999
100	1	0.08 ± 0.03	116.7 ± 8.6	(3.54 ± 0.01) × 10^{9}	0.39 ± 0.03	0.92 ± 0.01	0.26 ± 0.03	0.9999
	2	0.13 ± 0.02	195.8 ± 27.4	(2.71 ± 0.04) × 10^{16}	3.68 ± 0.15	0.46 ± 0.06	–3.50 ± 0.15	0.9996
	3	0.08 ± 0.01	256.5 ± 12.8	(1.15 ± 0.02) × 10^{21}	1.37 ± 0.10	0.69 ± 0.04	–1.12 ± 0.10	0.9994
	4	0.59 ± 0.06	348.3 ± 29.2	(2.00 ± 0.02) × 10^{28}	–0.37 ± 0.04	1.10 ± 0.02	0.58 ± 0.04	0.9999
	5	0.12 ± 0.02	264.9 ± 40.3	(3.52 ± 0.02) × 10^{20}	1.35 ± 0.05	0.91 ± 0.02	–1.09 ± 0.04	0.9999

[a] Average over $0.1 \leq \alpha_i \leq 0.9$

[b] Determination coefficient of the nonlinear least-squares analysis for the fitting of the kinetic curve using SB(m, n, p).

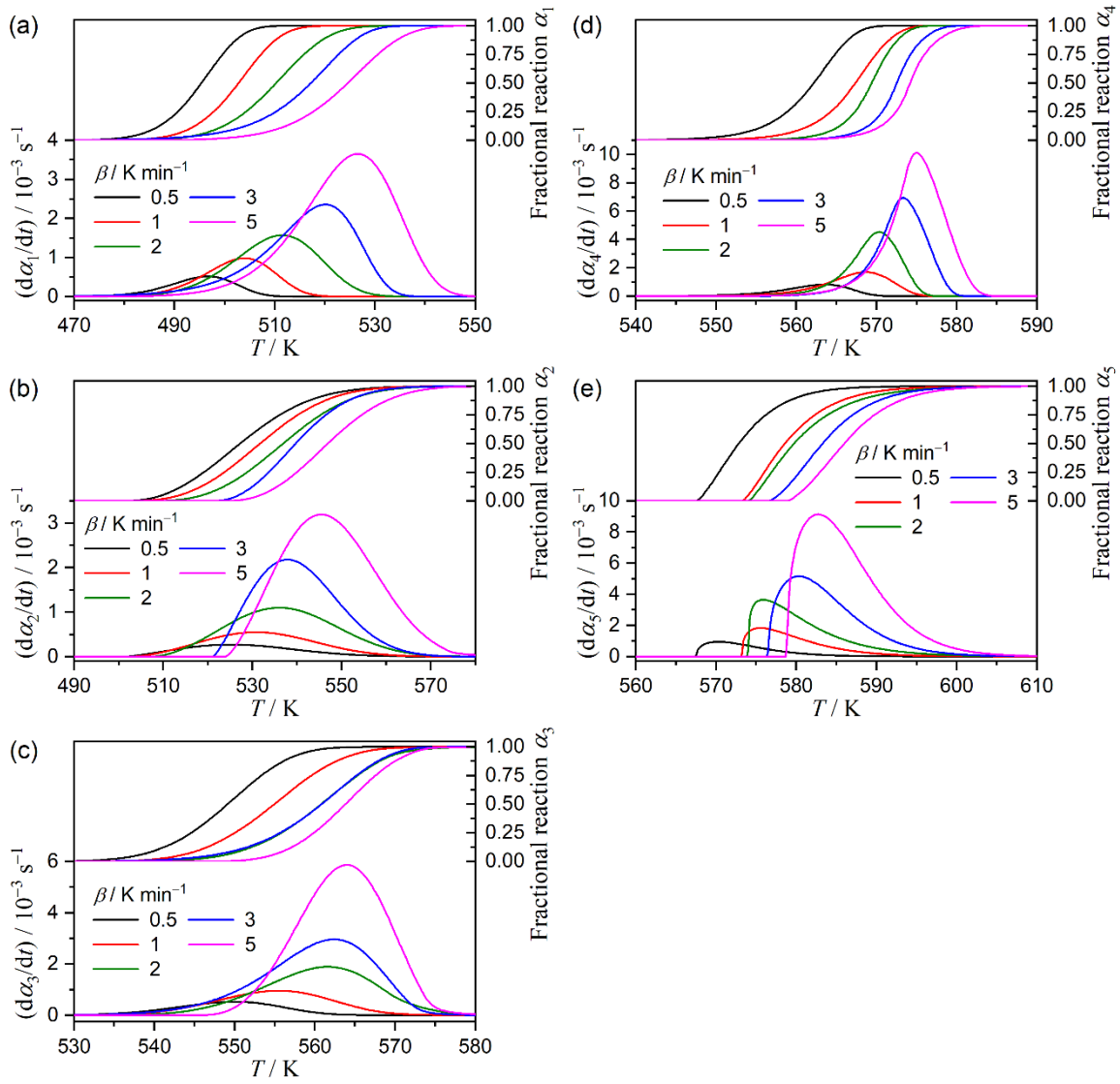

Figure S39. Kinetic curves for each component reaction step of the thermal decomposition of the granular malachite under linear nonisothermal conditions at $p(CO_2)$ = 5.0 kPa: (a) first, (b) second, (c) third, (d) fourth, and (e) fifth reaction steps.

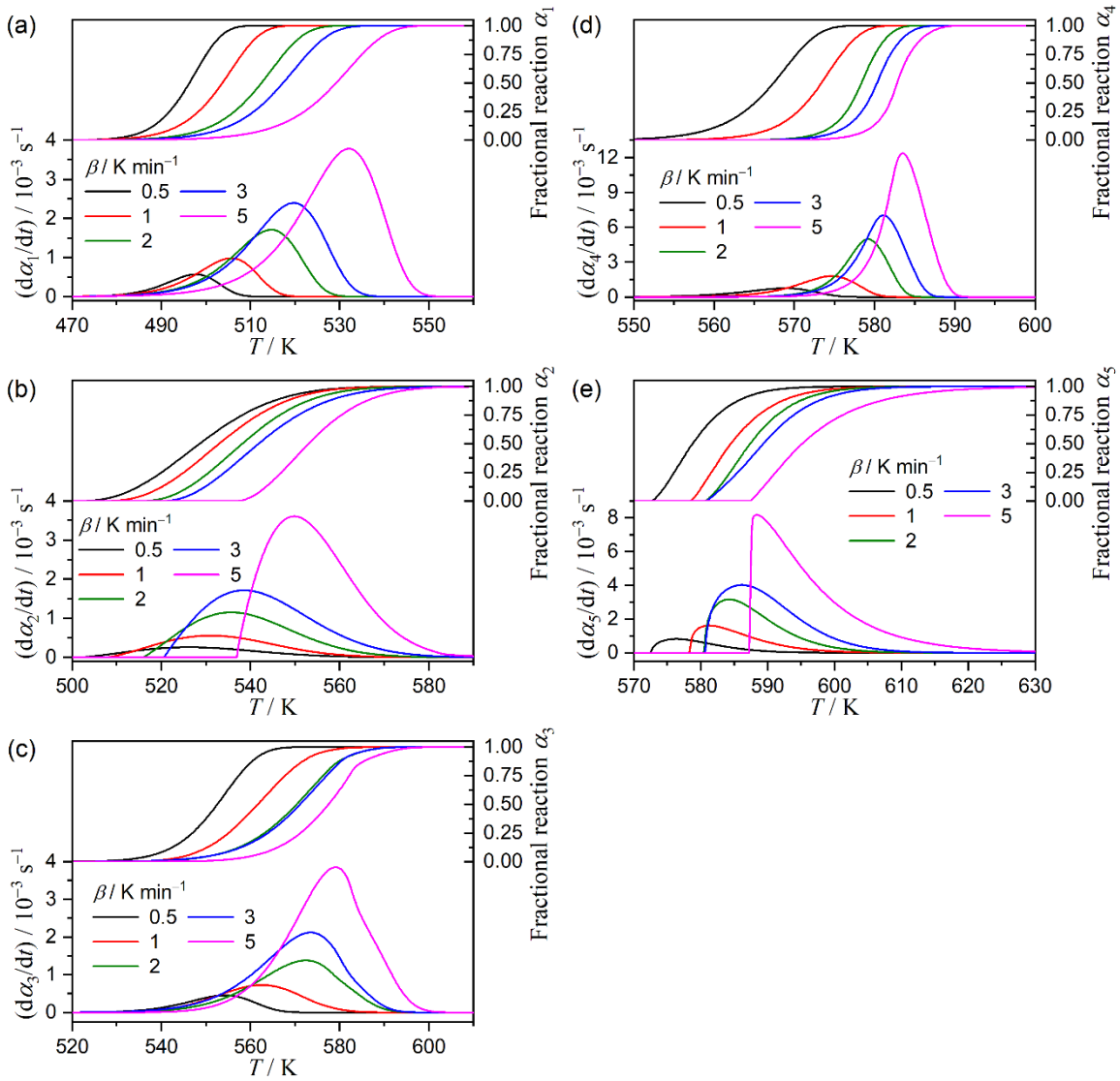

Figure S40. Kinetic curves for each component reaction step of the thermal decomposition of the granular malachite under linear nonisothermal conditions at $p(CO_2)$ = 10.0 kPa: (a) first, (b) second, (c) third, (d) fourth, and (e) fifth reaction steps.

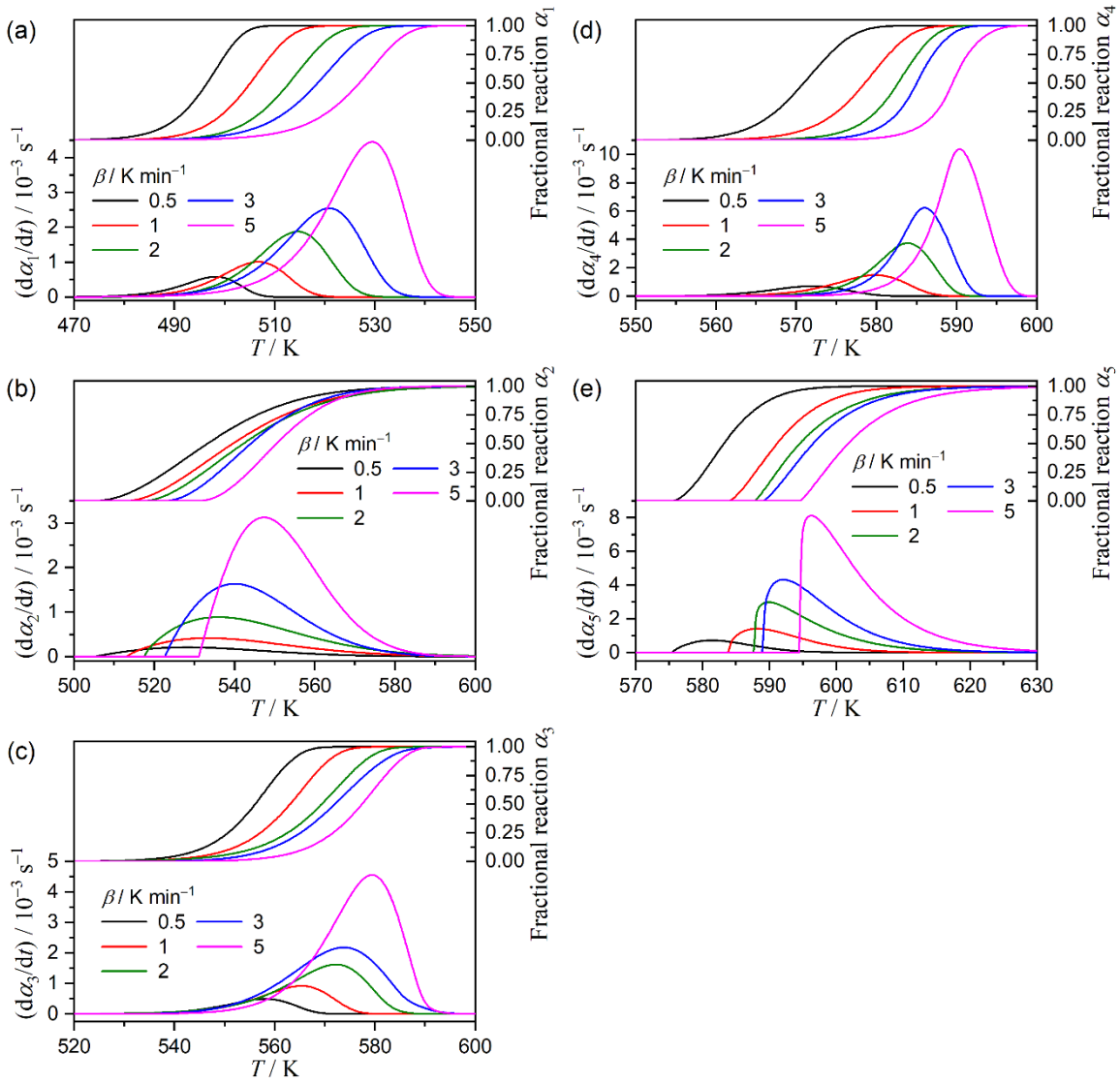

Figure S41. Kinetic curves for each component reaction step of the thermal decomposition of the granular malachite under linear nonisothermal conditions at $p(CO_2)$ = 20.0 kPa: (a) first, (b) second, (c) third, (d) fourth, and (e) fifth reaction steps.

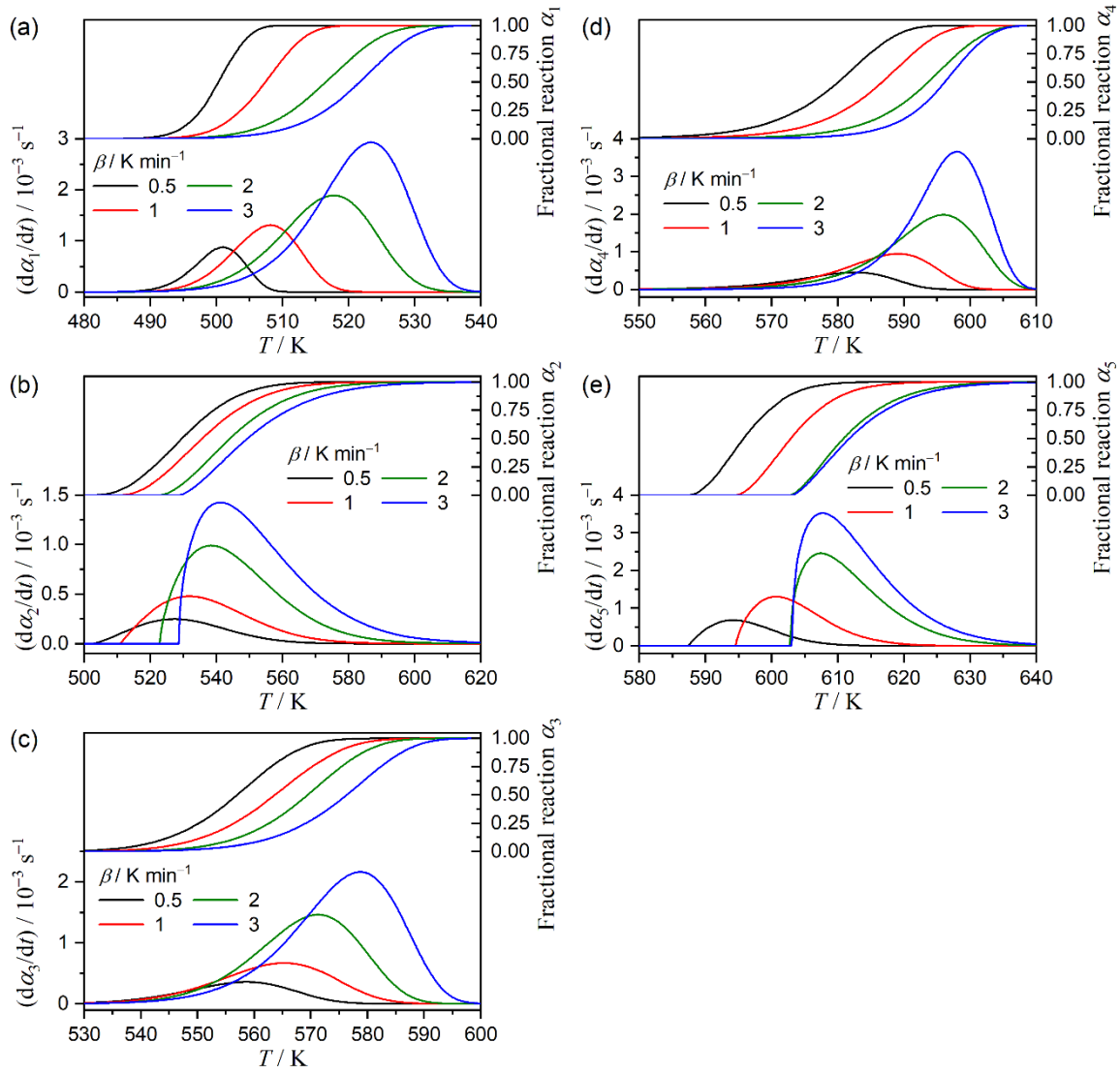

Figure S42. Kinetic curves for each component reaction step of the thermal decomposition of the granular malachite under linear nonisothermal conditions at $p(CO_2)$ = 100 kPa: (a) first, (b) second, (c) third, (d) fourth, and (e) fifth reaction steps.

The mathematically separated kinetic curves for each reaction step were analyzed using the Friedman plots as shown in Figures S43–S46 for the reactions at $p(CO_2)$ = 5.0, 10.0, 20.0, and 100 kPa, respectively. Figures S47–S50 show the $E_{a,i}$ values at different α_i and the experimental master plot calculated using the average $E_{a,i}$ value ($0.1 \leq \alpha_i \leq 0.9$) for each reaction step of the thermal decomposition of granular malachite at different $p(CO_2)$ values of 5.0, 10.0, 20.0, and 100 kPa, respectively. The experimental master plots were fitted using SB(m, n, p) model to obtain the A_i values and kinetic exponents (m_i, n_i, p_i). Table S4 lists the kinetic parameters estimated by the formal kinetic analysis for the mathematically separated kinetic curves.

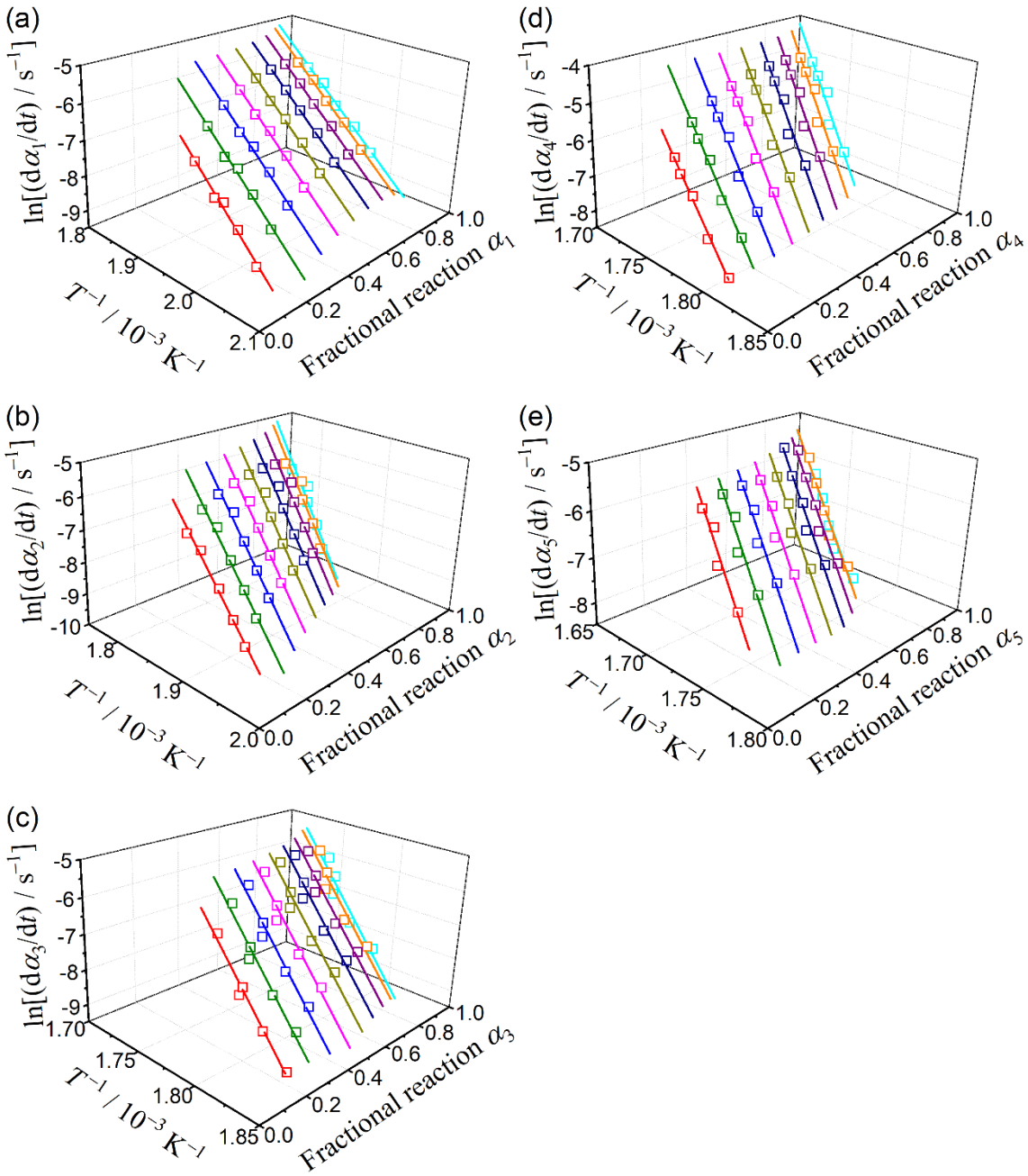

Figure S43. Friedman plots for each reaction step of the thermal decomposition of granular malachite at $p(CO_2)$ = 5.0 kPa: (a) first, (b) second, (c) third, (d) fourth, and (e) fifth reaction steps.

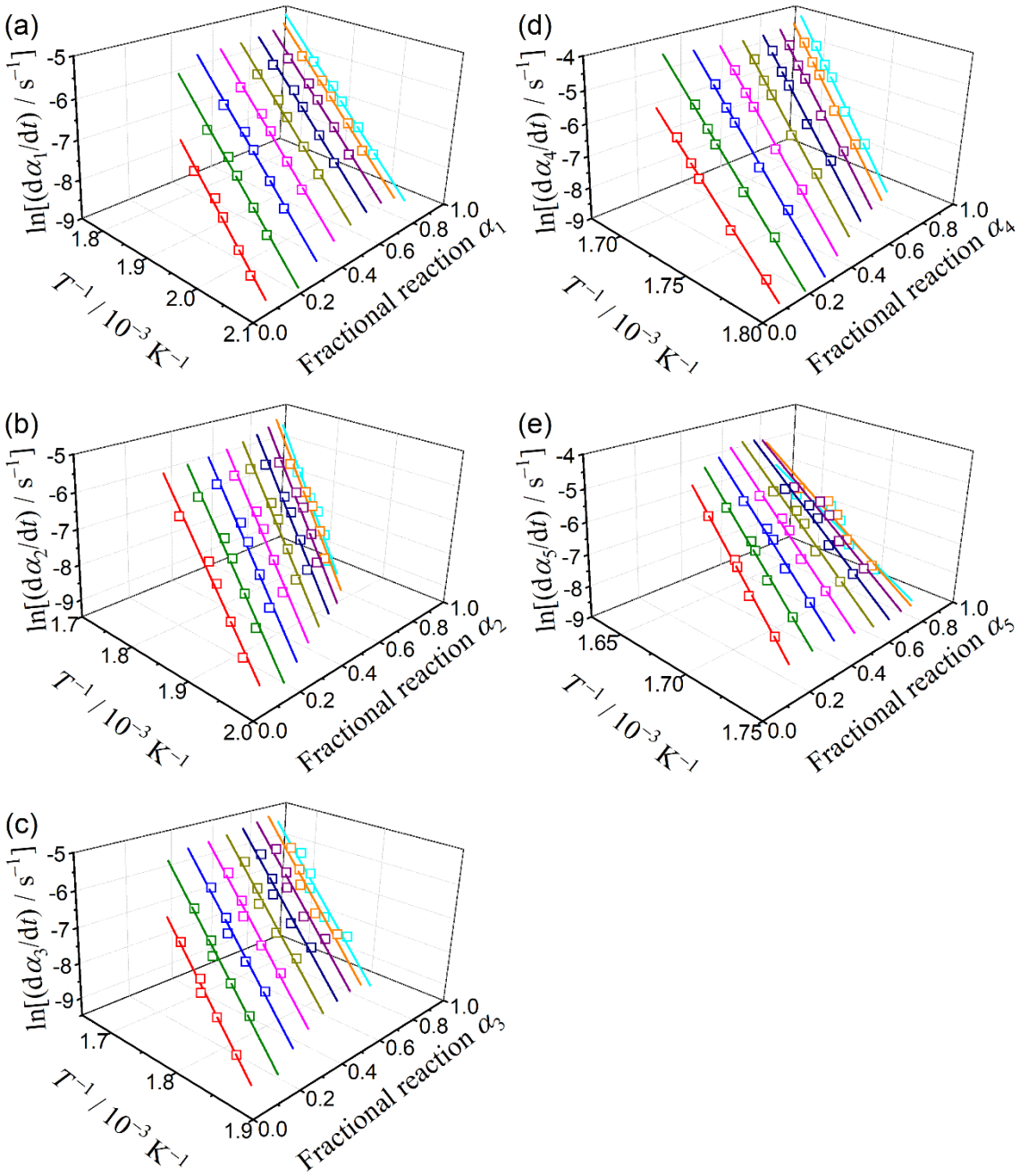

Figure S44. Friedman plots for each reaction step of the thermal decomposition of granular malachite at $p(CO_2)$ = 10.0 kPa: (a) first, (b) second, (c) third, (d) fourth, and (e) fifth reaction steps.

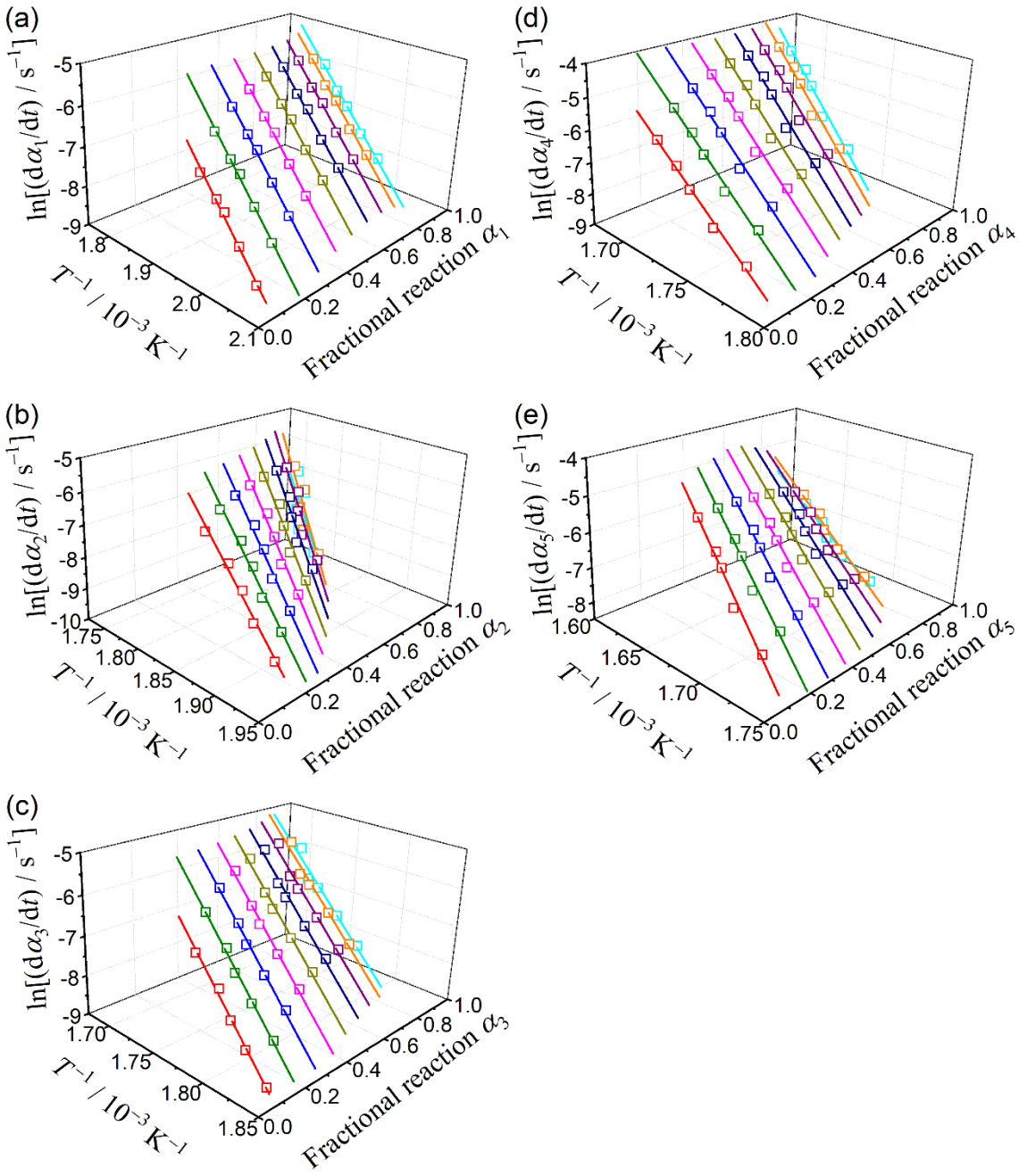

Figure S45. Friedman plots for each reaction step of the thermal decomposition of granular malachite at $p(CO_2)$ = 20.0 kPa: (a) first, (b) second, (c) third, (d) fourth, and (e) fifth reaction steps.

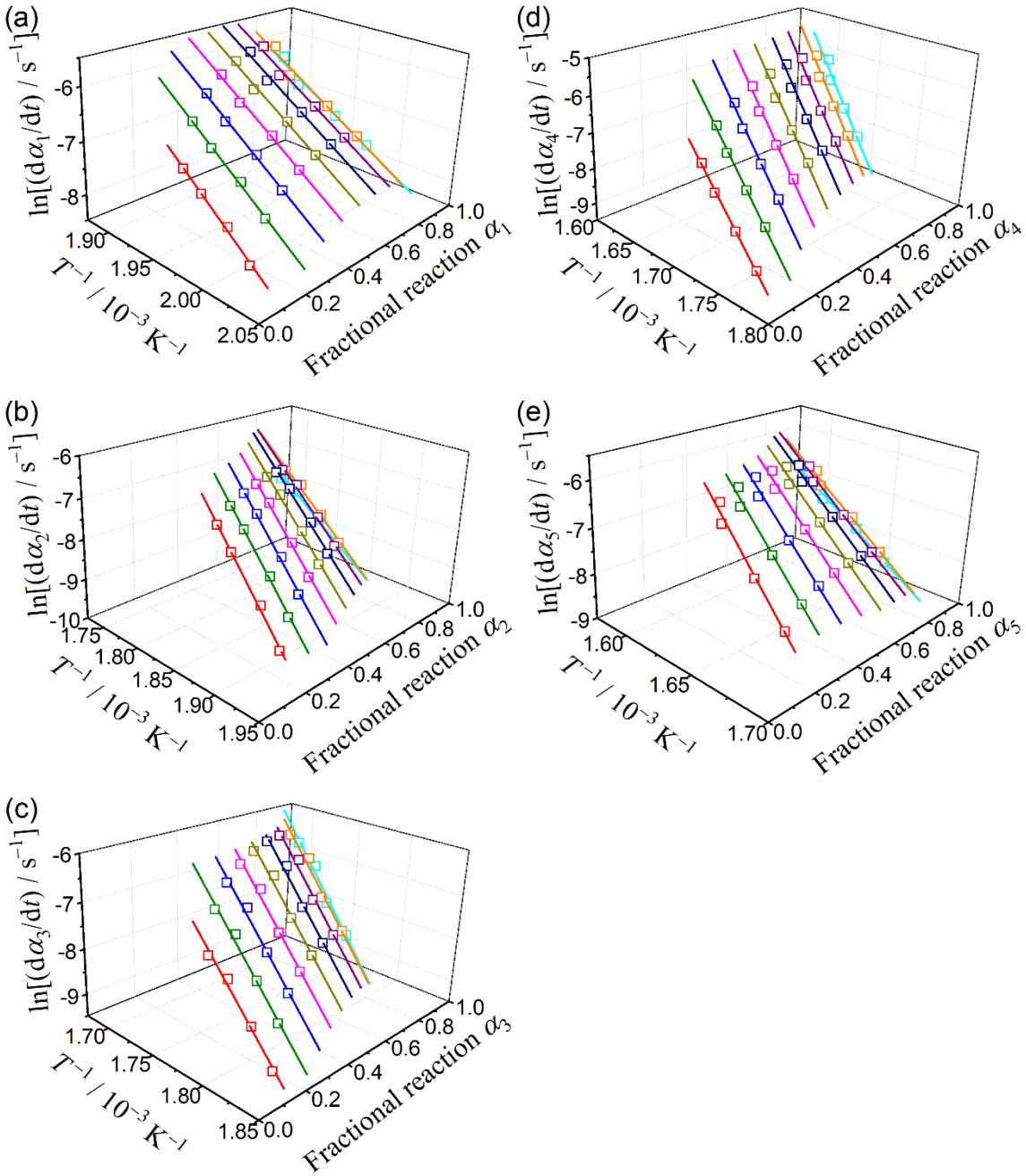

Figure S46. Friedman plots for each reaction step of the thermal decomposition of granular malachite at $p(CO_2)$ = 100 kPa: (a) first, (b) second, (c) third, (d) fourth, and (e) fifth reaction steps.

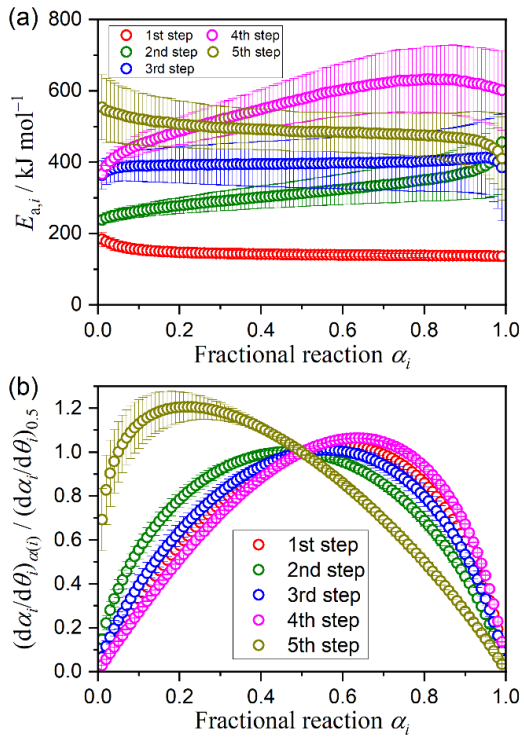

Figure S47. Kinetic results for each reaction step of the thermal decomposition of the granular malachite at $p(CO_2)$ = 5.0 kPa: (a) $E_{a,i}$ values at different α_i and (b) experimental master plots of $(d\alpha_i/d\theta_i)_{\alpha(i)}/(d\alpha_i/d\theta_i)_{0.5}$ versus α_i.

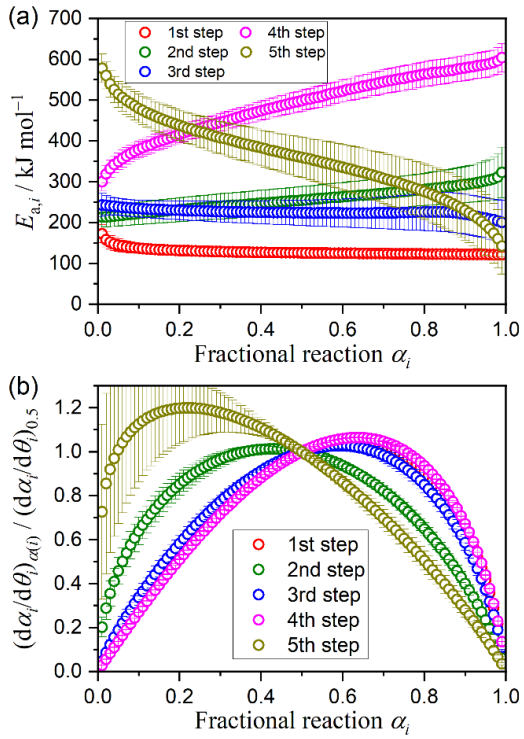

Figure S48. Kinetic results for each reaction step of the thermal decomposition of the granular malachite at $p(CO_2)$ = 10.0 kPa: (a) $E_{a,i}$ values at different α_i and (b) experimental master plots of $(d\alpha_i/d\theta_i)_{\alpha(i)}/(d\alpha_i/d\theta_i)_{0.5}$ versus α_i.

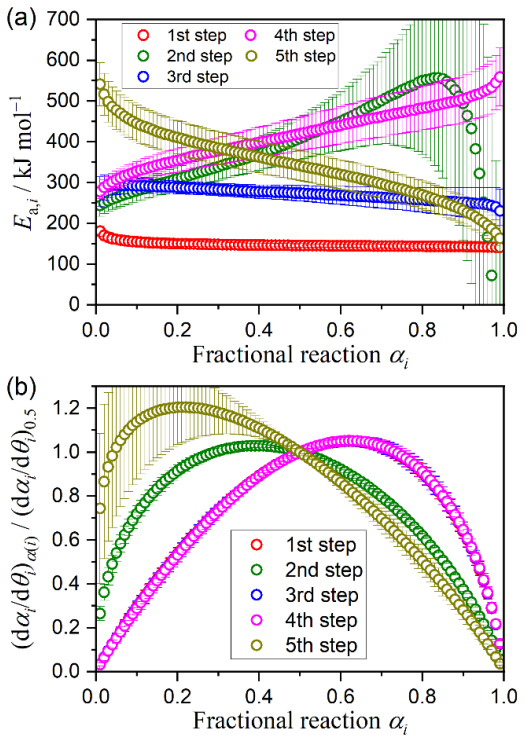

Figure S49. Kinetic results for each reaction step of the thermal decomposition of the granular malachite at $p(CO_2)$ = 20.0 kPa: (a) $E_{a,i}$ values at different α_i and (b) experimental master plots of $(d\alpha_i/d\theta_i)_{\alpha(i)}/(d\alpha_i/d\theta_i)_{0.5}$ versus α_i.

Figure S50. Kinetic results for each reaction step of the thermal decomposition of the granular malachite at $p(CO_2)$ = 100 kPa: (a) $E_{a,i}$ values at different α_i and (b) experimental master plots of $(d\alpha_i/d\theta_i)_{\alpha(i)}/(d\alpha_i/d\theta_i)_{0.5}$ versus α_i.

S3-3. Kinetic deconvolution analysis

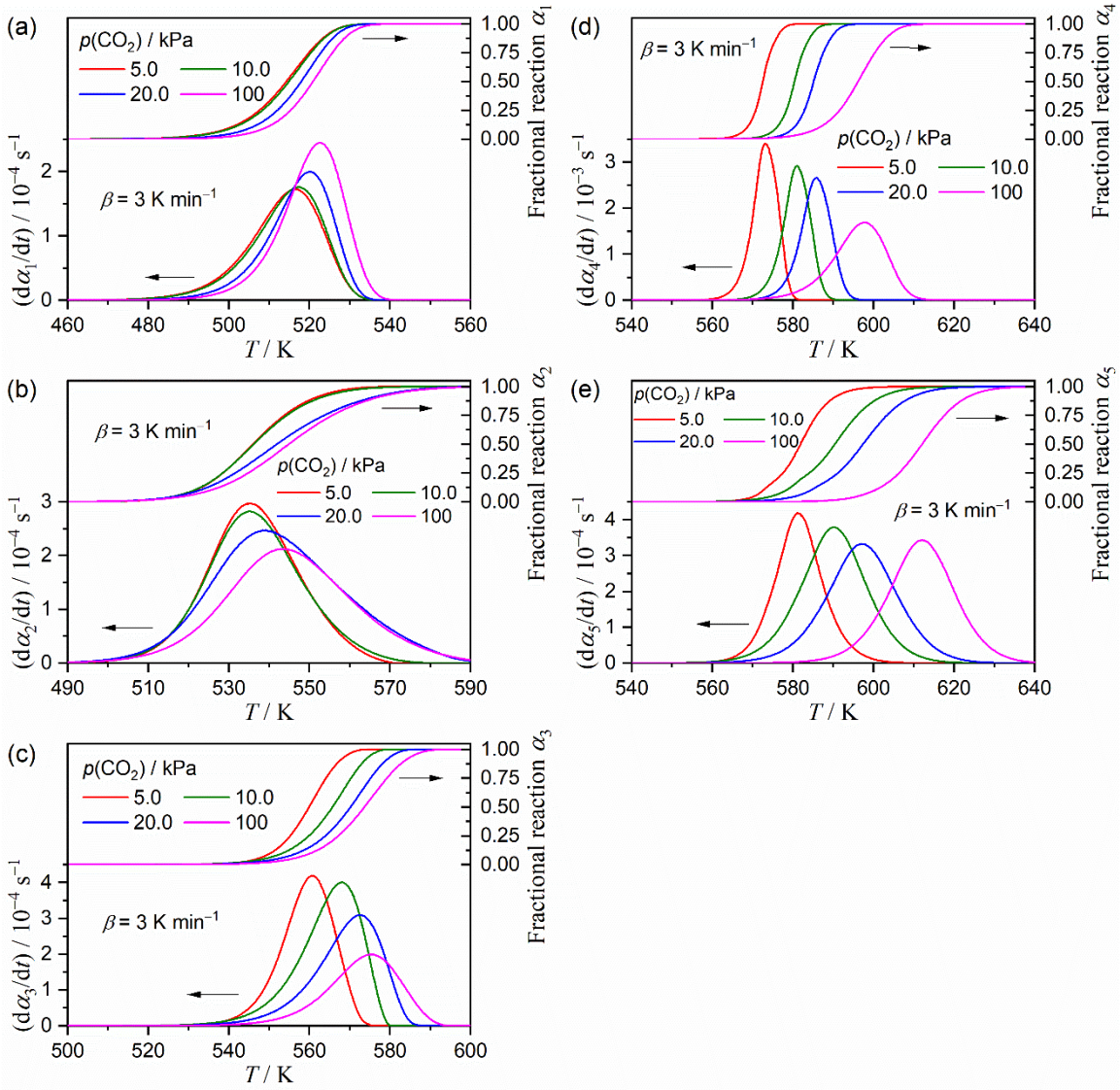

Figure S51. Kinetic curves at different $p(CO_2)$ values in each reaction step of the thermal decomposition of the granular malachite under linear nonisothermal conditions at a β of 3 K min^{-1}, extracted via KDA: (a) first, (b) second, (c) third, (d) fourth, and (e) fifth reaction steps.

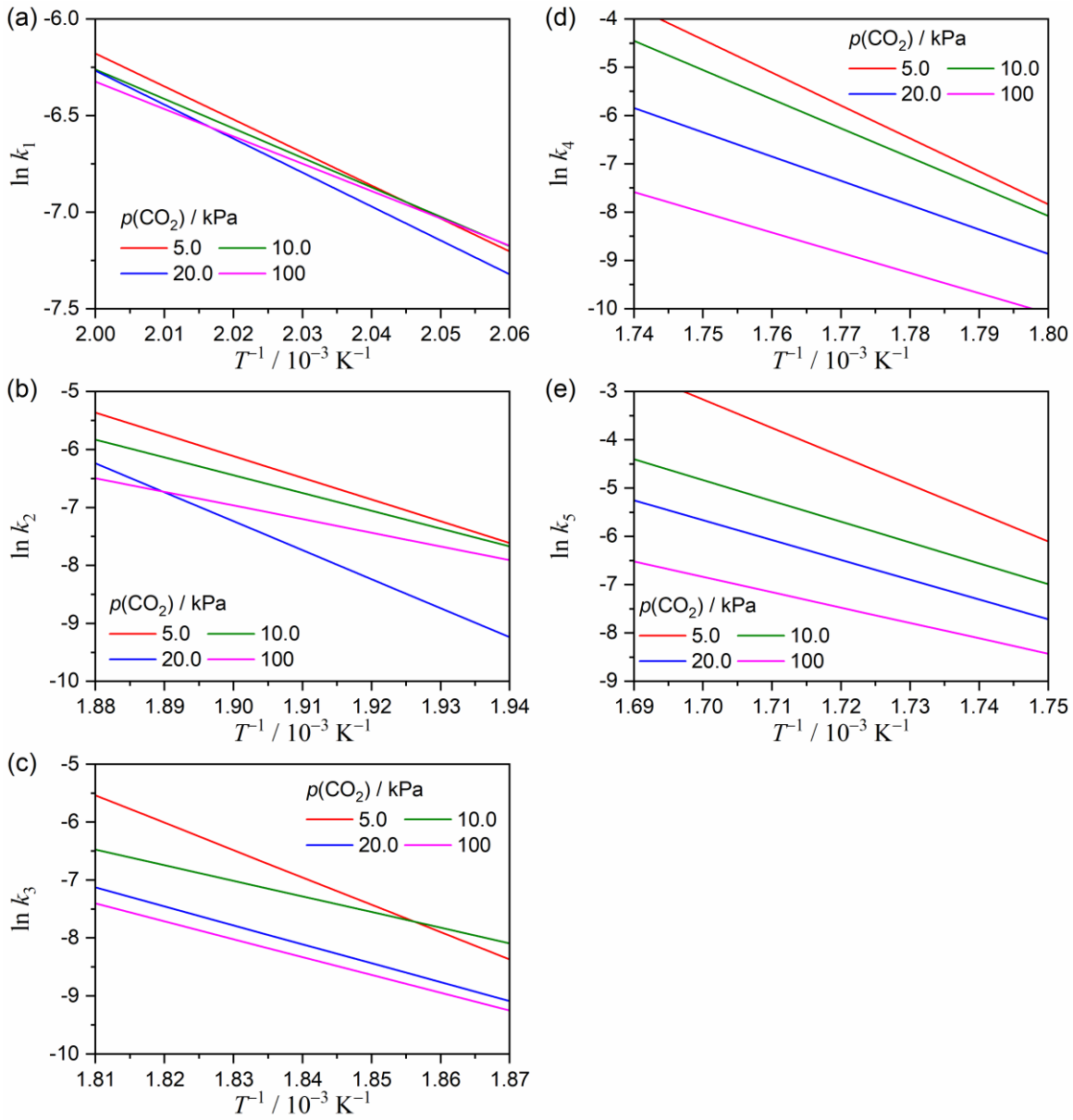

Figure S52. Arrhenius plots at different $p(CO_2)$ values in each reaction step of the thermal decomposition of the granular malachite, drawn using the Arrhenius parameters optimized via KDA: (a) first, (b) second, (c) third, (d) fourth, and (e) fifth reaction steps.